12-15-2020

Human pluripotent stem cell-derived kidney organoids with improved collecting duct maturation and injury modeling

Kohei Uchimura

Haojia Wu

Yasuhiro Yoshimura

Benjamin D Humphreys

Cell Reports

Article

Human Pluripotent Stem Cell-Derived Kidney Organoids with Improved Collecting Duct Maturation and Injury Modeling

Graphical Abstract

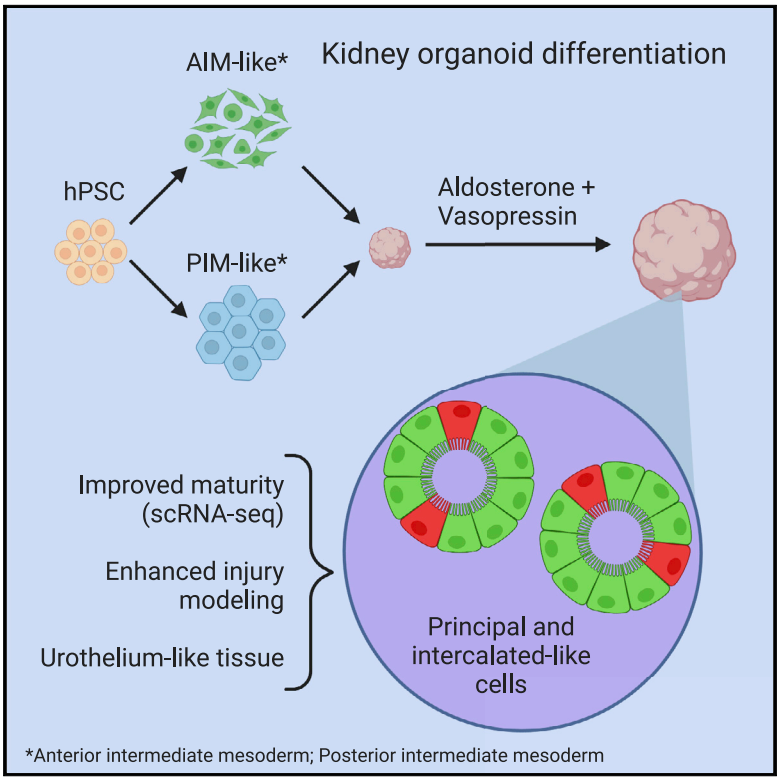

Highlights

- Combining differentiated progenitors leads to kidney organoids with collecting duct
- Aldosterone and vasopressin drive principal and intercalated cell differentiation
- Organoids show improved maturation and model tubular injury
- Notch regulates principal:intercalated cell ratios

Authors

Kohei Uchimura, Haojia Wu, Yasuhiro Yoshimura, Benjamin D. Humphreys

Correspondence

humphreysbd@wustl.edu

In Brief

Uchimura et al. combine independently differentiated metanephric mesenchyme-like and ureteric bud-like progenitors to generate human kidney organoids with a collecting system. Hormones aldosterone and arginine vasopressin drive principal and intercalated cell maturation, and Notch signaling could regulate cell ratios. Organoids also showed improved maturation and injury modeling.

Uchimura et al., 2020, Cell Reports *33*, 108514
December 15, 2020
https://doi.org/10.1016/j.celrep.2020.108514

CellPress

Cell Reports

CellPress
OPEN ACCESS

Article

Human Pluripotent Stem Cell-Derived Kidney Organoids with Improved Collecting Duct Maturation and Injury Modeling

Kohei Uchimura,[1] Haojia Wu,[1] Yasuhiro Yoshimura,[1] and Benjamin D. Humphreys[1,2,3,*]
[1]Division of Nephrology, Department of Medicine, Washington University School of Medicine, St. Louis, MO, USA
[2]Department of Developmental Biology, Washington University School of Medicine, St. Louis, MO, USA
[3]Lead Contact
*Correspondence: humphreysbd@wustl.edu
https://doi.org/10.1016/j.celrep.2020.108514

SUMMARY

Maximizing the potential of human kidney organoids for drug testing and regenerative medicine and to model development and disease requires addressing cell immaturity, the lack of a mature collecting system, and off-target cell types. By independently generating two kidney progenitor cell populations—metanephric mesenchyme and ureteric bud (UB)-like cells—we could generate kidney organoids with a collecting system. We also identify the hormones aldosterone and arginine vasopressin (AVP) as critical to promote differentiation of collecting duct cell types including both principal cells (PCs) and intercalated cells (ICs). The resulting PCs express aquaporin-2 (AQP2) protein, which undergoes translocation to the apical membrane after vasopressin or forskolin stimulation. By single-cell RNA sequencing (scRNA-seq), we demonstrate improved proximal tubule maturation and reduced off-target cell populations. We also show appropriate downregulation of progenitor cell types, improved modeling of tubular injury, the presence of urothelium (Uro), and the ability of Notch pathway modulation to regulate PC:IC ratios during organoid development.

INTRODUCTION

Substantial progress has been made in the development of protocols to differentiate human pluripotent stem cells (hPSCs) into kidney organoids. By manipulating Wingless-related integration site (Wnt) fibroblast growth factor (FGF), and transforming growth factor β (TGF-β) pathways, hPSCs are induced to differentiate into intermediate mesoderm and subsequently both the metanephric mesenchyme and ureteric bud (UB), which self-organize to form nephrons containing many kidney cell types (Freedman et al., 2015; Morizane et al., 2015; Taguchi et al., 2014; Takasato et al., 2014; Xia et al., 2014). Modifications of the original protocols have improved results, for example, the use of VEGF, shear stress, or transplantation into immunodeficient mice to induce vascularization (Czerniecki et al., 2018; Homan et al., 2019; van den Berg et al., 2018). Variability in organoid differentiation between batch and cell line is now increasingly recognized as is the presence of off-target cell populations (Phipson et al., 2019; Subramanian et al., 2019; Wu et al., 2018). We have recently shown that single-cell RNA sequencing (scRNA-seq) can reveal signaling pathways whose inhibition reduces the differentiation of off-target cells (Wu et al., 2018).

However, limitations to current kidney organoid differentiation protocols remain. While recent genetic lineage analysis indicates that UB derivatives are present in some kidney organoids (Howden et al., 2019), until recently other investigators have been unable to identify definitive UB lineage (Subramanian et al., 2019) including principal cell (PC) markers such as aquaporin-2 (AQP2) as well as acid- and base-secreting intercalated cells (ICs) (Czerniecki et al., 2018). Recently Taguchi and Nishinakamura (2017) showed that mouse embryonic stem cells (ESCs) can be induced to form kidney organoids with a properly branched UB-derived collecting system by inducing metanephric mesenchyme and UB separately and then recombining them. This protocol required the concurrent addition of primary stromal progenitors isolated from developing mouse kidney, however, precluding its application to human kidney organoids.

Another limitation of current protocols is the relative immaturity of all kidney cell types generated, which resemble first- and second-trimester fetal kidney rather than differentiated cell types (Subramanian et al., 2019; Takasato et al., 2016; Wu et al., 2018). Fetal kidney cells may not be well suited to model disease or epithelial function.

Mae et al. (2018) reported a protocol for the induction of UB from hPSCs. Based on that work, Tsujimoto et al. (2020) recently reported a system for separate induction of mesodermal progenitors from hPSCs. After combination, the resulting organoids generated glomeruli and tubules as well as collecting duct and could become vascularized after transplantation *in vivo*. Here, we establish a different protocol for the separate induction of both metanephric mesenchyme and UB-like progenitors from hPSCs. Combination of these progenitors results in collecting duct-like structures that, with the addition of the hormones vasopressin and aldosterone, develop both PCs and ICs expressing

terminal differentiation markers. Other tubular segments also exhibited enhanced maturation, including vasopressin-induced membrane translocation of AQP2 protein and appropriate induction of injury markers in response to cisplatin. We could also detect for the first time urothelial (Uro) cells and could shift the ratio of PCs and ICs by modulating Notch signaling.

RESULTS

Separate Induction toward Metanephric Mesenchyme and UB Improves Collecting Duct Branching

We primarily used the induced PSC (iPSC) line BJFF.6 for these studies. Having previously shown by scRNA-seq that hPSCs differentiated using the Takasato protocol to day 7 most closely resemble posterior intermediate mesoderm (PIM), we followed this protocol for PIM induction (Wu et al., 2018). In order to generate anterior intermediate mesoderm (AIM) in parallel, we made modifications to the Nishinakamura protocol (Taguchi and Nishinakamura, 2017). We accomplished mesoderm induction with 3 days of exposure to the Wnt agonist CHIR99021 (CHIR) rather than 1.5 days, delayed addition of activin and BMP4 until day 1, and omitted the TGF-β receptor (TGF-βR) inhibitor SB431542 entirely. We also observed improved tubulogenesis in joint culture when AIM induction included heparin and activin at later stages (data not shown). The PIM and AIM induction schemes are shown in Figure 1A.

We monitored the expression of AIM versus PIM markers over time by qPCR. AIM markers *LHX1*, *EMX2*, and *GATA3* were appropriately induced in AIM (Figure 1B), and PIM markers *GDNF*, *T*, *SIX2*, and *HOXA11* were appropriately expressed in PIM (Figure 1C). Immunofluorescence analysis revealed strong expression of the AIM marker *GATA3* in AIM, but not PIM, and conversely strong expression of the PIM marker *HOXD11* in PIM, but not AIM (Figures 1D and S1A). Based on this limited panel of markers, these results suggest that we were able to differentiate AIM-like and PIM-like progenitors.

At day 7, cells were dissociated from monolayer culture and mixed at ratios from 3:1 to 1:3 followed by a CHIR pulse for 1 h. For the next 5 days, the combined organoids were incubated in a cocktail including FGF9, heparin, glial-cell-line-derived neurotrophic factor (GDNF), retinoic acid, and epidermal growth factor (EGF) (Figure 1A). Organoids were left to mature in basal medium without growth factors from day 12 to day 26, similar to prior protocols. Both the 1:1 and 1:3 ratios (PIM:AIM) showed some evidence of keratin 8 (CK8)-positive branched structures at day 26; these ratios were used for further studies (Figure S1B). Of note, AIM cultured alone for the whole protocol did not lead to the differentiation of lotus tetragonolobus lectin (LTL)-positive proximal tubule (Figure S1B).

Aldosterone and Vasopressin Drive Collecting Duct Maturation

Despite the improved UB patterning with this protocol, markers of PC differentiation such as AQP2 were undetectable (data not shown), as has been observed in other organoid differentiation protocols (Czerniecki et al., 2018; Subramanian et al., 2019). Recently, important roles for the circulating hormone triiodothyronine in cell specification of human retinal organoids were reported (Eldred et al., 2018). We therefore considered whether other circulating hormones that act specifically on PCs might aid in cell maturation. Exposure to angiotensin-converting enzyme inhibitors during pregnancy is associated with congenital anomalies and particularly renal tubular dysgenesis (Gubler, 2014), suggesting that the renin-angiotensin-aldosterone axis might regulate tubulogenesis. Arginine vasopressin (AVP), also known as antidiuretic hormone, is another circulating hormone that regulates PC water permeability and induces AQP2 transcription (Ecelbarger et al., 1997; Nielsen et al., 1993; Pearce et al., 2015), providing further rationale to test its role in PC maturation.

To test the role of aldosterone and AVP in collecting duct maturation, we compared day 12 to day 26 in basal medium alone versus 10 nM aldosterone and 10 nM AVP. We also included 100 nM K252a, an inhibitor of neurotrophic receptor tyrosine kinase 2, since we have shown that this reduces off-target neurons by 90% (Wu et al., 2018). This is a lower concentration than our original report because we observed smaller organoids at higher concentrations in this protocol; however, we could document that the lower dose still inhibited off-target neuronal differentiation (Figure S2A). Inclusion of the hormones strongly induced the expression of PC maturation markers including *AQP2*, *SCNN1G*, and *KCNJ1* as reflected by bulk qPCR. It also upregulated IC markers (*AQP6*, *ATP6V1B1*, and *CLCNKA*), a cell type not previously reported in kidney organoids (Figure 1E). Both aldosterone and vasopressin were required for the full effect (Figure S2B). By contrast, exposure of organoids generated in our laboratory by the Takasato protocol to the same conditions from day 12 to day 26 did not result in the generation of PC or IC types (Figures S3A and S3B). These results suggested that aldosterone and AVP drove maturation of both PC and IC types. We observed qualitatively similar results in the human ESC (hESC) line H9 (Figures S3C and S3B).

Enhanced Collecting Duct Cell Maturation

We next assessed cell type diversity by immunofluorescence analysis. AQP2 protein could be detected on a subset of the collecting duct marker dolichos bifloris agglutinin (DBA)-positive cells (Figure 2A). These cells were scattered within the presumptive UB lineage. We could also detect the protein product of *ATP6V1B1*, the B1 subunit of the v-type proton ATPase, in a separate subset of collecting duct cells, indicating the emergence of IC types. All other major kidney cell types could be detected as well, including proximal tubule (LTL), distal tubule (E-cadherin and SLC12A1), podocytes (WT1 and NPHS1), endothelium (platelet endothelial cell adhesion molecule-1, CD31), and stroma (MEIS1 and PDGFRB) (Figure 2A).

We confirmed that AQP2 was co-expressed within the GATA3-positive collecting duct population, and we could not detect AQP2 protein in the GATA3 population from Takasato organoids (Figure 2B). In organoids differentiated with the current protocol, larger duct-like structures could be seen emerging from areas of tubulogenesis, whereas such duct-like structures were absent from Takasato organoids. By immunofluorescence analysis, these larger ducts were GATA3 positive, contained a scattered AQP2-positive cell population, and emerged from

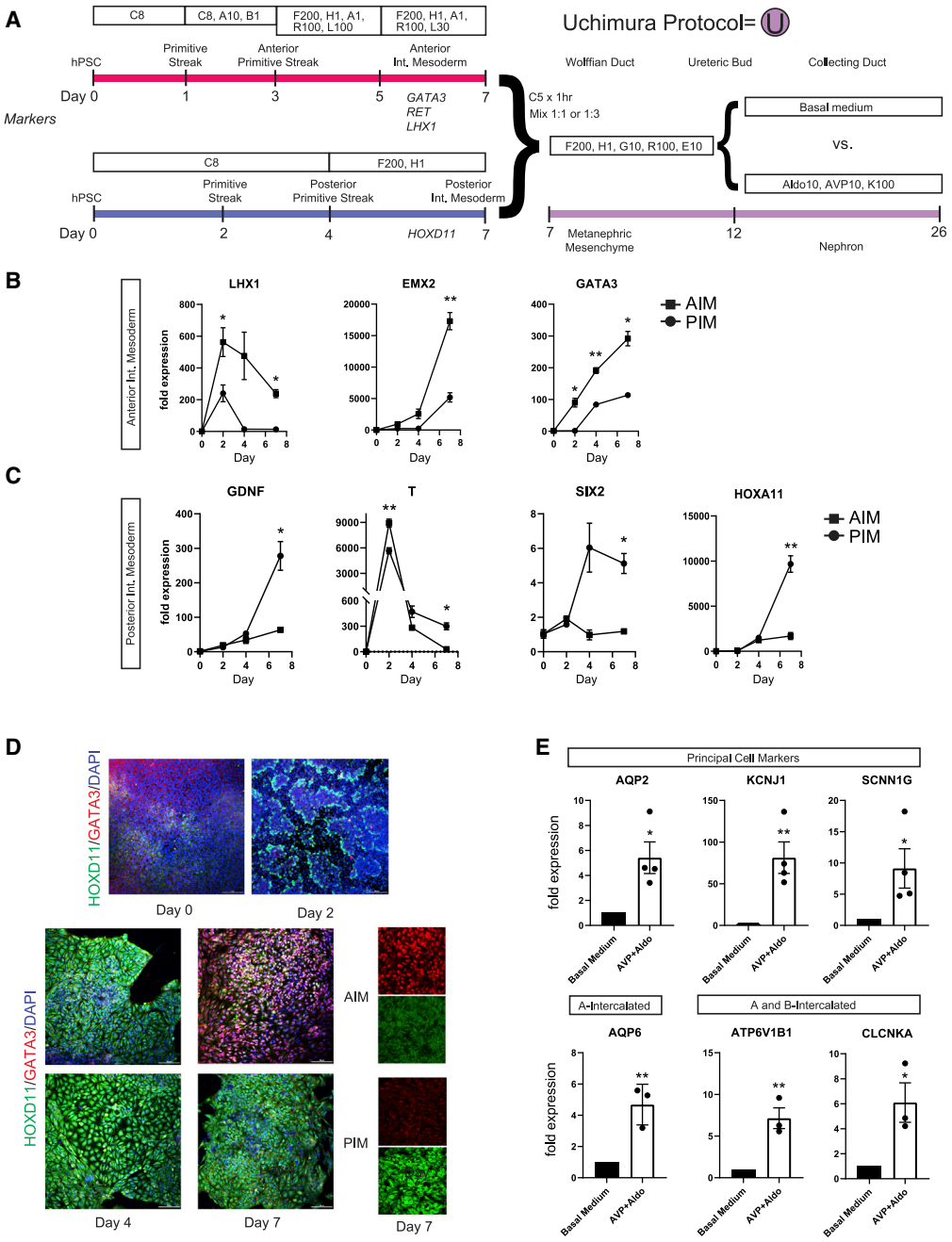

Figure 1. Separate Induction of Anterior and Posterior Intermediate Mesoderm and Effect of Aldo and Vasopressin on Collecting Duct (CD) Maturation

(A) Outline of the Uchimura protocol. A, activin (ng/mL); Aldo, aldosterone (nM); AVP, arginine vasopressin (nM); B, BMP (ng/mL); C, CHIR (μM); E, EGF (ng/mL); F, FGF9 (ng/mL); G, GDNF (ng/mL); H, heparin (μg/mL); K, K252a (nM); LDN, LDN193189 (nM); SB, SB431542 (μM); R, 0.1 mM retinoic acid; Y, 10 μM Y27632.

(B and C) Temporal kinetics of AIM and PIM marker gene expression during the first week of differentiation by qPCR (n = 3).

(D) Fluorescence images of AIM marker GATA3 compared with PIM marker HOXD11 during initial differentiation. Scale bars, 100 μm.

(E) Maturation of organoids between day 12 and day 26 in basal medium versus Aldo10, AVP10, and K100 reveals much greater induction of principal cell (PC) as well as intercalated cell (IC) markers in the latter condition (qPCR; n = 3–4). *$p < 0.05$ and **$p < 0.01$.

the center of the organoid extending to proximal tubules located on the organoid periphery (Figures S4A–S4C; Videos S1 and S2).

To better visualize collecting duct organization, we performed whole-mount immunofluorescence analysis on cleared organoids from both protocols stained with the proximal tubule marker

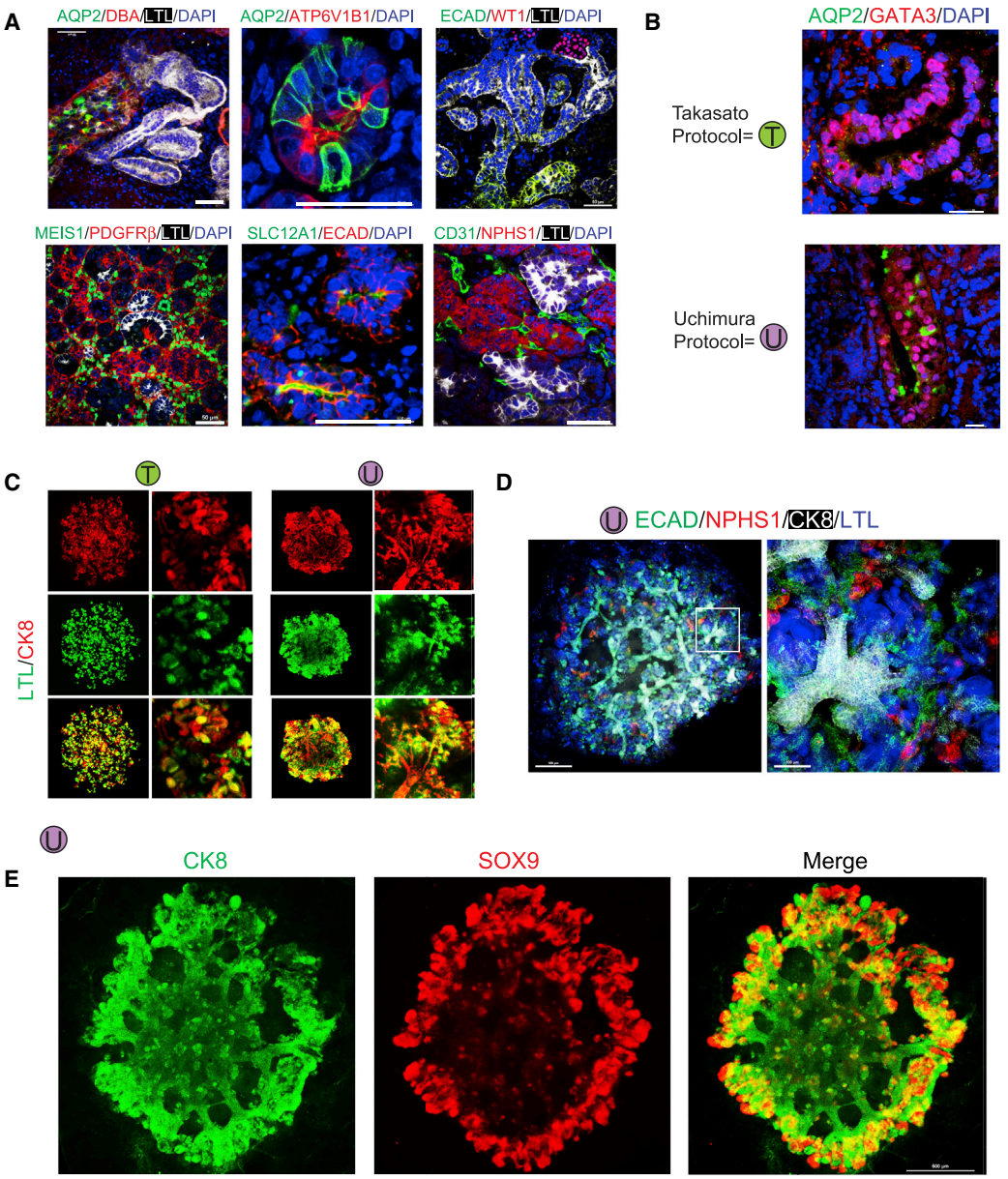

Figure 2. Characterization of Organoid CD Development and Differentiation

(A) Fluorescence images from day 26 organoids including Aldo and vasopressin show the presence of major kidney cell types, including PCs (AQP2 and DBA) and ICs (ATP6V1B1). Scale bars, 50 μm.

(B) Fluorescence images showing that Uchimura protocol organoids generate GATA3 and AQP2 copositive CD cells, whereas AQP2 expression is not detectable in Takasato organoids. Scale bars, 20 μm.

(C) Comparison of CK8-positive tubule organization in Takasato versus Uchimura organoids.

(D) Whole mount showing glomeruli and proximal tubules on periphery and CD located in the central region. Scale bar, 100 μm.

(E) Whole-mount images of CK8-positive CD with SOX9-positive ureteric bud (UB) tips at periphery. Scale bar, 500 μm.

LTL and the UB marker CK8. Organoids differentiated with the Takasato protocol showed localized proximal tubules with adjacent UB structures in a random pattern (Figure 2C). By contrast, the current protocol was characterized by glomeruli and proximal tubules on the periphery of the organoid, with CK8-positive collecting duct structures in the center (Figure 2D). There was a modest degree of UB branching that could be visualized by whole-mount *CK8* staining. Of note, UB tips selectively expressed *SOX9*, suggesting the existence of both *SOX9*$^{+}$ ureteric tip and *SOX9*$^{-}$ stalk (Figure 2E).

We next measured maturation markers in organoids generated with our protocol compared with organoids generated in our laboratory using the Takasato protocol. Comparison of polarized expression of basolateral Na/K/ATPase and apical LTL revealed

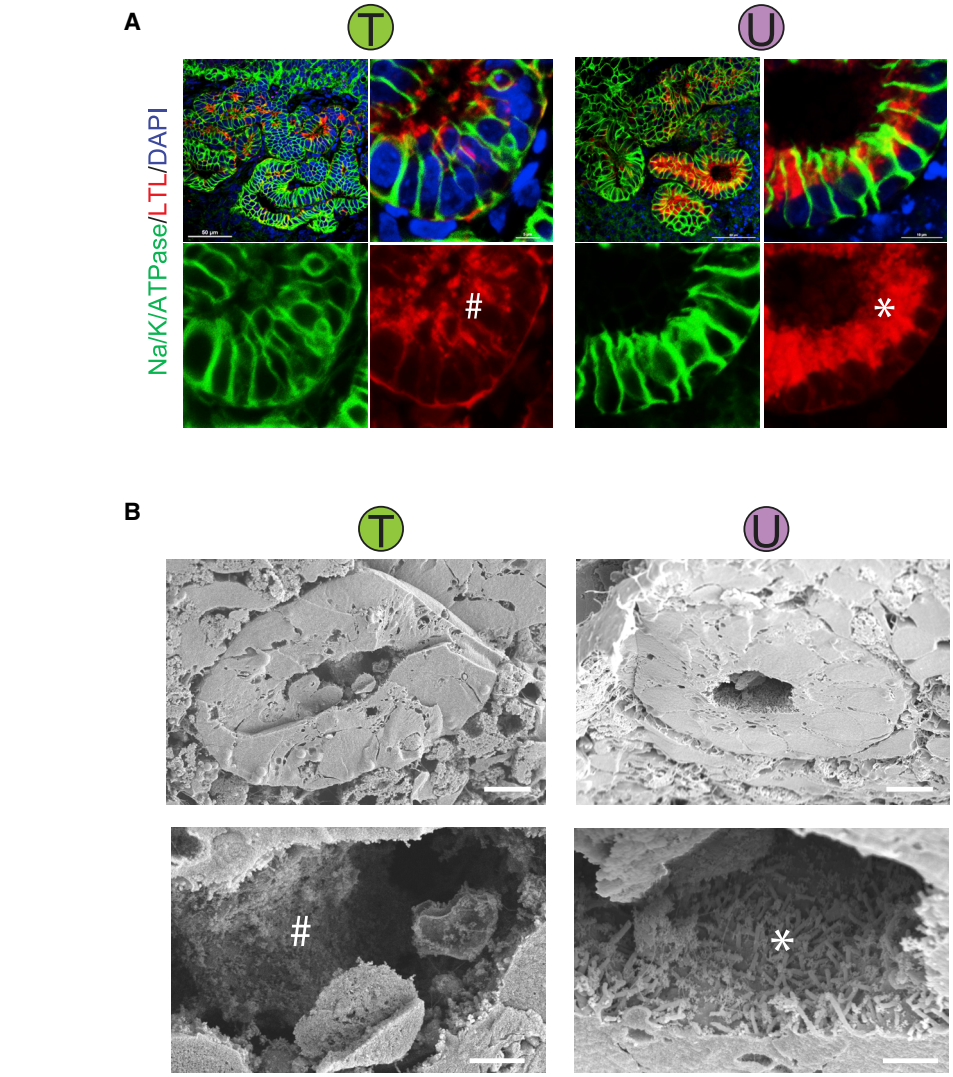

(legend on next page)

denser apical expression of LTL in proximal tubules differentiated using the current protocol (Figure 3A). This was confirmed by scanning electron microscopy where proximal tubule from our protocol had a higher microvillus density (Figure 3B). Consistent with this finding, there was much higher mRNA for the proximal tubule gene *SLC34A1* in our organoids than for those generated by us with the Takasato protocol as measured by qPCR (Figure 3C). There was also decreased *SIX2* expression, suggesting differentiation of metanephric mesenchyme. While the podocyte marker *NPHS1* was unchanged, there was increased expression of thick ascending limb marker *SLC12A1* and the distal convoluted tubule markers *SLC12A3* and *CALB1* (Figure 3C). Also consistent with our earlier observations, we could measure substantially increased *AQP2* expression and expression of IC markers *SCNN1G*, *ATP6V1B1*, and *AQP6* in organoids generated with the current protocol compared with those generated with the Takasato protocol. Expression of stromal markers was also modestly elevated (Figure 3C).

scRNA-Seq to Define Cell Diversity and Maturity

In order to comprehensively investigate cell diversity in organoid cell types, we performed scRNA-seq using the 10x Genomics platform. After quality control filtering, we obtained 16,939 cells from day 26 kidney organoids from our protocol and compared them with 19,015 cells generated in parallel from the original Takasato protocol (Takasato et al., 2016). We performed integrative analysis on both datasets using Harmony, an algorithm that enables joint analysis of separate datasets (Korsunsky et al., 2019). Unsupervised graph-based clustering of the combined datasets followed by post hoc annotation of the clusters defined a total of 13 major organoid cell types with highly consistent expression patterns across protocols (Figures 4A and 4D). This included one glomerular cell type expressing typical podocyte markers (*PODXL* and *NPHS2*), two mesenchymal cell types, two tubular cell types transcriptomically resembling the fetal proximal tubule and loop of Henle (Figure S5), one cluster expressing collecting duct markers (*GATA3* and *AQP2*), and seven non-renal cell types (Figures 4A and 4D). Each kidney cell type contained cells from both protocols (indicating that technical variations were regressed out by Harmony) but with varying proportions (suggesting that biological differences were retained) (Figures 4B and 4C). Although we could detect rare endothelial cells by immunofluorescence, these did not form an independent cluster from either protocol, indicating that our adaptation of the Takasato protocol may have differences in cell composition from what was originally reported (Takasato et al., 2015).

Consistent with the immunofluorescence and qPCR results (Figure 1), our modified protocol generated a greater number of cells categorized as collecting duct (8-fold more compared with the Takasato protocol) (Figure 4C). This PC population comprised ~28% of the organoid, and 53% of these cells expressed AQP2. Our protocol also reduced the number of off-target cells by 4.6-fold, most likely because we included BDNF signaling pathway inhibition (Figures 4C and S2A) (Wu et al., 2018). These results were confirmed by performing independent clustering on each dataset (Figures 4E and 4F). We could detect greater expression of *GATA3* in cells from our protocol than from the Takasato protocol. *AQP2* expression was absent from Takasato organoids (Figures S4D–S4G).

We next quantified the degree of maturation of organoid-derived PCs by comparing them with their fetal and adult counterparts (Figures S5A–S5C) (Hochane et al., 2019; Wu et al., 2018). In order to simplify the comparison, we also selected only PCs in which AQP2 expression was detected. Projecting the cell source onto the clusters showed that nearly all (95.2%) of the organoid-derived PCs clustered with fetal and not adult PCs (Figure 4G). Dotplot visualization of selected differentially expressed genes confirmed the fetal nature of organoid-derived PCs (Figure 4H). We also selected a set of marker genes for PCs based on analysis of existing adult human kidney scRNA-seq and compared relative expression of these between PCs from our protocol versus the Takasato protocol. This showed increased markers of PC maturation in our protocol as well as persistent expression of developmental markers in Takasato protocol PCs (Figures S5D and S5E).

Our bulk mRNA analysis indicated higher expression of proximal tubule maturation markers in our protocol, so we next quantified their maturation state using the scRNA-seq datasets. Subclustering of all proximal tubules from both protocols identified three proximal tubule subtypes whose separation was primarily driven by the degree of maturation (Figure 4I). For example, two of the three clusters expressed cell-cycle and progenitor marker genes. More than 75% of the proximal tubule cells from our protocol were grouped into the mature proximal tubule cluster, whereas >65% of the Takasato protocol proximal tubule cells were grouped in the two immature clusters (Figure 4J). In line with this finding, the current protocol proximal tubule cell expressed higher mature markers (*DAB2*, *ALDH1*, *CUBN*, and *LRP2*), whereas the Takasato protocol proximal tubule cells strongly expressed cycling genes (*MKI67*, *CENPF*, and *HMGB2*) and tubular progenitor markers (*CCND1*, *PAX2*, and *LHX1*) (Figure 4K).

hPSC-Derived Kidney Organoids Contain Uro

Our protocol generated a substantial number of collecting duct cells (28.5% of the total), so we next asked whether separate cellular subtypes might exist within this lineage. A second

Figure 3. Assessment of Organoid Maturation

(A) LTL staining suggests that proximal tubule possesses a more developed LTL-positive brush border (*) compared with Takasato organoids (#). Scale bar, 50 μm in low-power images and 10 μm in high-power images.

(B) Scanning electron micrographs comparing proximal tubules from Takasato and Uchimura protocols. Relatively few microvilli are visible in the Takasato organoid (#), whereas microvillus density is higher in Uchimura protocol organoids (*). Representative images from n = 3 biologic replicates. Scale bar, 5 μm in top images and 1 μm in bottom images.

(C) Comparison of the average expression of marker genes and developmental genes between organoid protocols (n = 5). *$p < 0.05$, **$p < 0.01$, ***$p < 0.001$, and ****$p < 0.0001$.

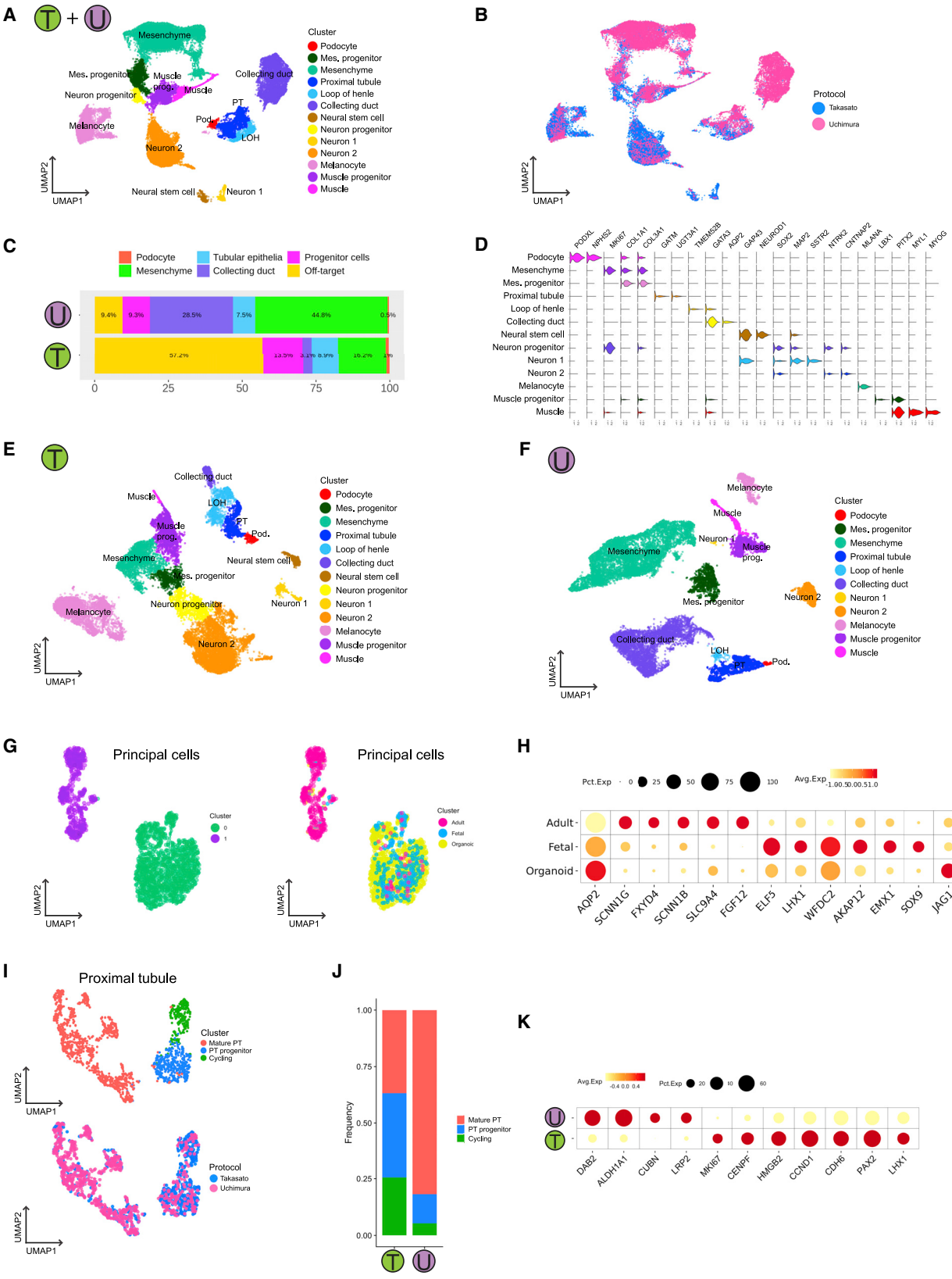

(legend on next page)

round of clustering on the collecting duct cluster revealed four distinct collecting duct subtypes including UB cells, PCs, ICs, and Uro cells (Figure 5A). Inspection of the gene expression unique to each subcluster confirmed the identity of each cell subtype (Figure 5B). Of note, some AQP2-positive PCs also expressed IC markers, suggesting that they may either represent PC-IC transition cells that have been previously described (Park et al., 2018), or alternatively, bipotential progenitor cells (Figure 5B).

Cells within a single lineage exist at different stages of differentiation within the same organoid. Since PC and IC derive from UB, we therefore performed pseudotime trajectory analysis on the UB, PC, and IC clusters. The pseudotime trajectory began with UB cells and subsequently bifurcated, leading either to PC or IC fate (Figure 5C). To identify candidate transcription factors driving PC and IC differentiation from UB, we inferred gene expression dynamics across pseudotime. Extracting transcription factors over this trajectory revealed 51 transcription factors (TFs) that were upregulated during PC/IC differentiation (Figures 5D and 5E; Table S1). These included transcription factors already known to be expressed in developing collecting duct or to regulate collecting duct fate and function such as *TFCP2L1* (Werth et al., 2017), *KLF6* (Fischer et al., 2001), *TOX3* (Harding et al., 2011), *FOXQ1* (Blomqvist et al., 2004), *PAX8* (Narlis et al., 2007), and *LHX1* (Kobayashi et al., 2005). To identify genes specific either to the PC or the IC branch, we performed branch analysis using the branched expression analysis modeling algorithm (BEAM) in Monocle (Qiu et al., 2017). This analysis generated 493 differentially expressed genes with the majority of these present in the IC trajectory (Table S2).

Uro cells have not been described in kidney organoids to date, but they do arise from UB progenitors, so we better characterized this cluster to distinguish it from collecting duct (Mendelsohn, 2009). Although some of the genes expressed in this cluster are also found in distal collecting duct (*UPK2* and *KRT7*), others are specific to Uro (*UPK1B*, *UPK3B*, *FAM46A*, and *CLIC*). To assign identity to the Uro cluster in an unbiased way, we mapped the Uro transcriptomes to lower tract cell types from the Human Cell Landscape in an unsupervised fashion (Han et al., 2020). The only cell types the organoid cluster mapped to were ureteric epithelium (Figure 5F), providing strong evidence for our Uro annotation. We also confirmed expression of UPK2 and KRT7 by immunofluorescence analysis. Organoid Uro cells were copositive for GATA3 and formed relatively wide linear structures without a discernible lumen (Figure 5G). We could not detect UPK2 expression in organoids differentiated by the Takasato protocol (Figures 5H and 5I). These results show that Uro cells are a genuine cell type present in our kidney organoids, indicating that kidney organoids hold potential for modeling ureteral development.

Modeling Tubular Injury, Collecting Duct Water Channel Translocation, and PC-IC Interconversion

Several groups have reported modest induction of apoptosis and kidney injury markers such as *HAVCR1* in response to tubular toxins (Czerniecki et al., 2018; Higgins et al., 2018; Morizane et al., 2015; Takasato et al., 2015), and the ability to faithfully model injury and repair in kidney organoids represents a goal for the field. Neutrophil gelatinase-associated lipocalin (NGAL) is an early biomarker for ischemic, septic, or nephrotoxic kidney injury that is expressed in both thick ascending limb and collecting duct and that to our knowledge has not been detected in kidney organoids (Paragas et al., 2011). Hepatitis A virus cellular receptor 1 (HAVCR1) is also induced by toxic or ischemic kidney injury specifically in the proximal tubule (Ichimura et al., 1998). The epithelial toxicant cisplatin induced both NGAL and HAVCR1 mRNA expression in organoids generated with our protocol (Figure 6A). We could also verify that apically located *HAVCR1* protein was induced specifically in LTL-positive proximal tubules, and *NGAL* protein was induced specifically in *ECAD*-positive distal tubules, as expected (Figure 6B). NGAL protein could also be detected by western blot (Figure S6A).

AVP-stimulated insertion of AQP2 into the apical membrane of the PC represents the primary mechanism by which the kidney regulates water balance in the body (Pearce et al., 2015). The ability to model this process in a kidney organoid where the local cellular and environmental cues more closely mimic the *in vivo* situation may provide insights compared with *in vitro* PC culture models. We subjected day 26 organoids to washout of aldosterone and AVP for 24 h, followed by stimulation with vehicle or 10 nM AVP for 3 h. AVP stimulation resulted in the translocation of AQP2 protein from a primarily cytosolic localization to the apical membrane (Figures 6C and S6B). AQP2 insertion into the apical membrane is dependent on cAMP-dependent protein kinase A (PKA) activation. We could also trigger translocation of cytosolic AQP2 protein to the plasma membrane in sorted DBA-positive cells by the adenylate cyclase agonist forskolin (Figure 6D).

The ratio of PCs to ICs in collecting duct is regulated during development by Notch signaling (Jeong et al., 2009). Interconversion of these cell types can also be induced by manipulating the Notch pathway in the adult, and cells undergoing this transition have been characterized by scRNA-seq (Park et al., 2018). To test whether the composition of collecting duct cell types

Figure 4. Comparison of Kidney Cell Types and Differentiation State in Takasato versus Uchimura Protocols

(A) Uniform manifold approximation and projection (UMAP) co-projection of scRNA-seq data from both the Takasato and Uchimura protocols.
(B) Assignment of protocol of origin to all cells reveals that most of the off-target cell types originated from the Takasato protocol.
(C) Comparison of percentage of cells across clusters between the two protocols.
(D) Violin plot showing marker gene expression for all cell types from both protocols.
(E and F) UMAP projection of the Takasato protocol organoids alone and expression of CD markers GATA3 and AQP2.
(G and H) UMAP projection of the Uchimura protocol and expression of GATA3 and AQP2.
(I) All proximal tubule cells from both protocols co-projected and identified by protocol (top) or by unsupervised clustering of the combined dataset (bottom).
(J) The Uchimura protocol had a larger proportion of mature proximal tubule and smaller proportion of progenitor and cycling proximal tubule cells.
(K) Dotplot comparing expression of proximal tubule maturation markers and developmental markers between the two protocols.

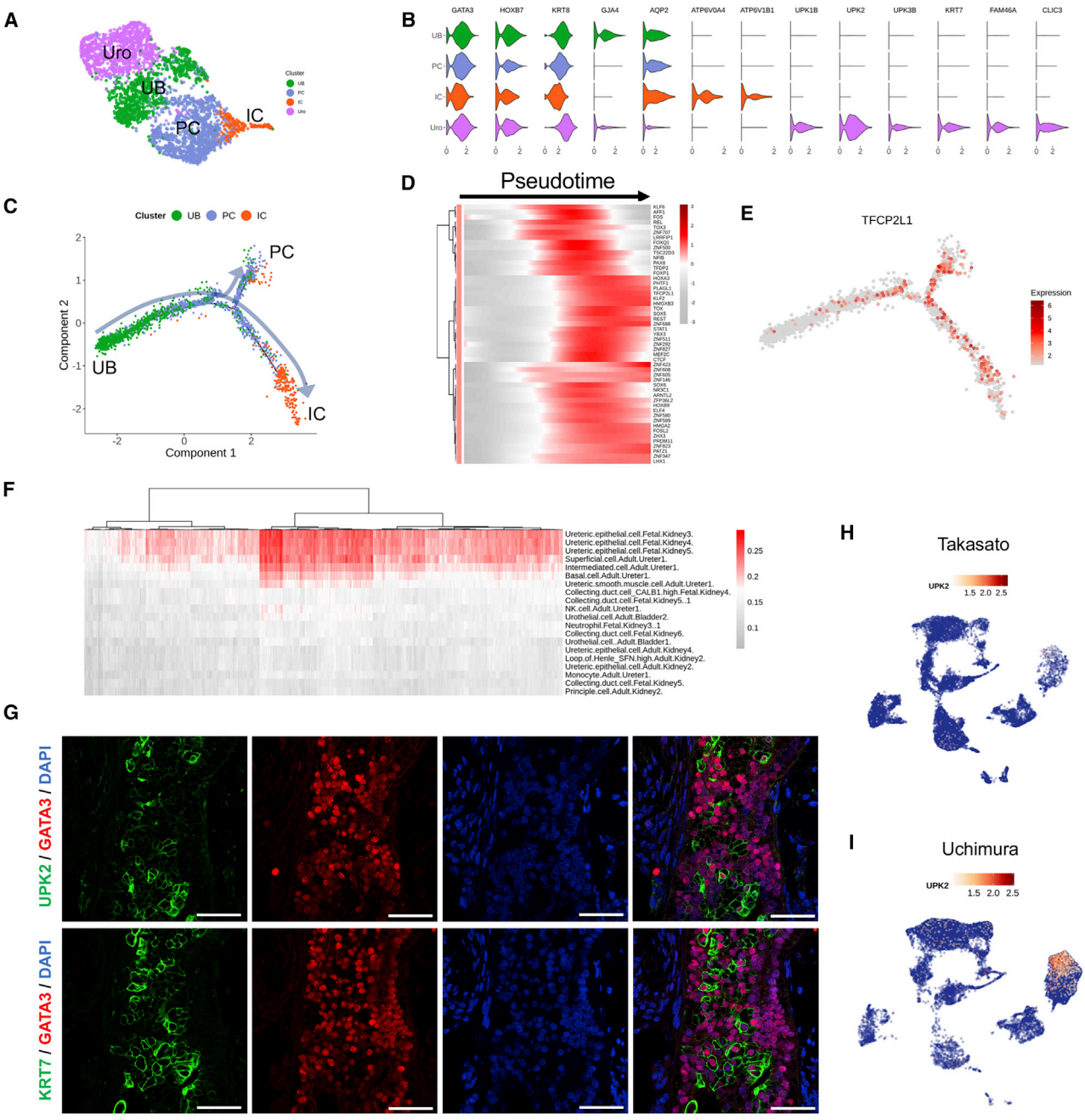

Figure 5. Heterogeneity of CD Cells Derived from This Protocol

(A) Four cell types were identified from subclustering analysis of the CD cells.

(B) Expression of known cell type markers in each cluster. Note that urothelial markers UPK1B and UPK2 were specifically expressed in the organoid urothelium.

(C) Pseudotime trajectory analysis revealed bifurcating differentiation trajectories of PC and IC.

(D) Differentially expressed genes across the PC and IC trajectories.

(E) Expression of transcription factor TFCP2L1 across pseudotime.

(F) Unsupervised analysis (Pearson correlation) comparing the organoid urothelial cluster to the top 20 most similar cell types from the Human Cell Landscape.

(G) Validation of urothelial marker gene expression by immunofluorescence. Scale bar, 50 μm.

(H and I) Comparison of UPK2 expression in the kidney organoids derived from Takasato and Uchimura protocols.

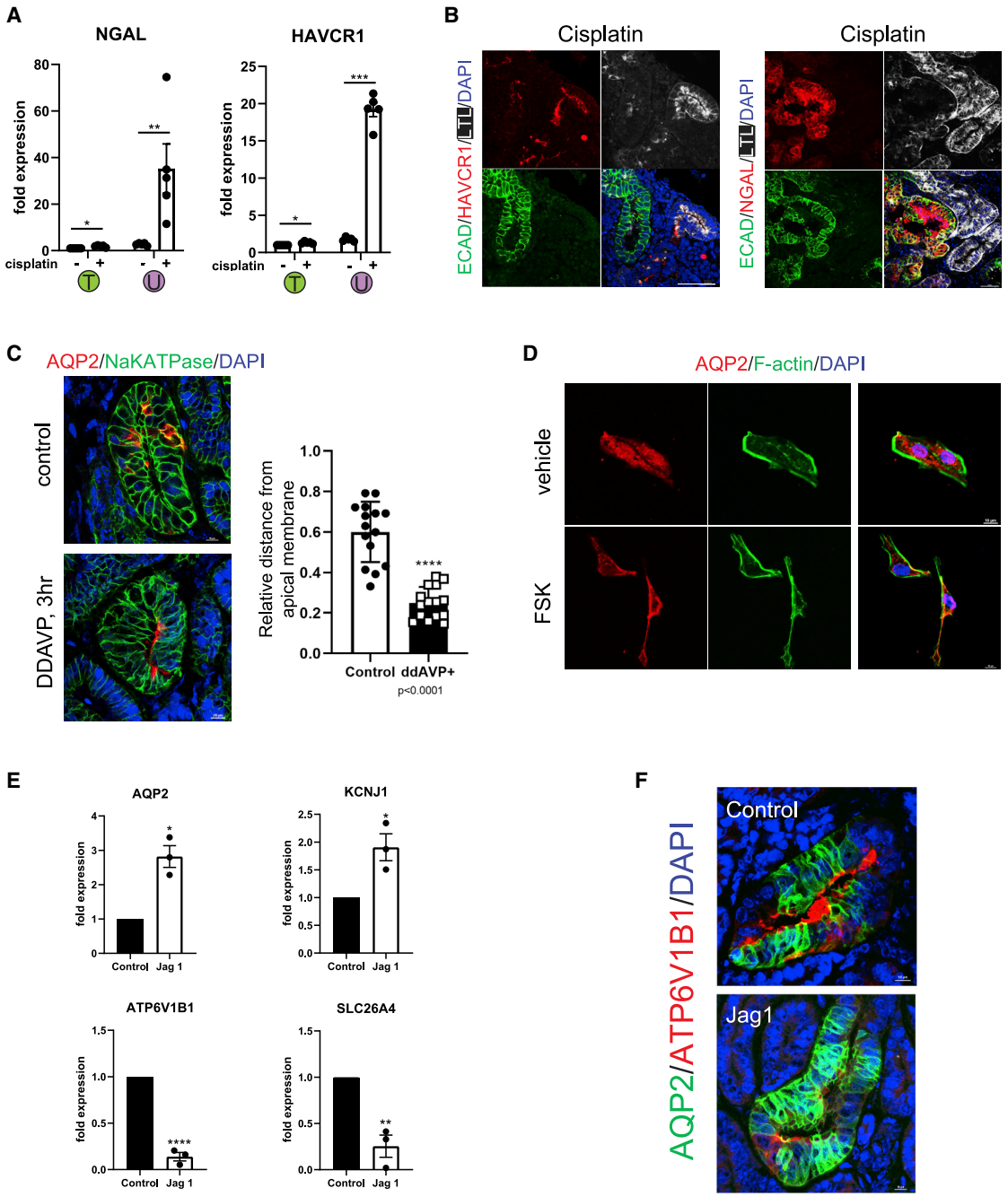

Figure 6. Organoid Injury Responses, Vasopressin-Stimulated AQP2 Insertion, and Regulation of PC and IC Ratio by Notch Pathway

(A) Upregulation of injury markers HAVCR1 and NGAL after by cisplatin in Uchimura, but not Takasato, organoids measured by qPCR (n = 5). Cisplatin was administered for 48 h from day 26 to day 28. *p < 0.05, **p < 0.01, and ***p < 0.001.

(B) Fluorescence images showing upregulation of the proximal tubule injury marker HAVCR1 in LTL-positive proximal tubule after cisplatin exposure and distal tubule injury marker NGAL in E-cadherin-positive distal tubules. Scale bars, 50 μm.

(C) Fluorescence images from whole Uchimura organoids incubated with vehicle or 10 nM AVP for 3 h after 24 h washout. AQP2 protein translocates to the apical surface (arrowhead) after AVP stimulation. Bar graph quantifies translocation. Scale bars, 10 μm. ***p < 0.001.

(D) Flow-sorted DBA^{+} cells were exposed to vehicle or forskolin (FSK). Fluorescence images reveal translocation of cytoplasmic AQP2 to the F-actin-positive plasma membrane after FSK stimulation. Scale bar, 10 μm. *p < 0.05.

(E) Relative mRNA levels of PC markers (*AQP2* and *KCNJ1*) and intercalated cell markers (*ATP6V1B1*, *CLCNKA*, and *SLC26A4*) from organoids treated with either vehicle or 100 ng/mL Jag1. *p < 0.05, **p < 0.01, and ****p < 0.001.

(F) Fluorescence images from organoids treated with either vehicle or 100 ng/mL Jag1. Scale bars, 10 μm.

could be manipulated during kidney organoid differentiation, we treated organoids with vehicle or the Notch agonist Jag1. By bulk qPCR, this manipulation increased expression of PC markers AQP2 and KCNJ1, while reducing expression of intercalated cell markers ATP6V1B1, CLCNKA, and SLC26A4 (Figure 6E). We confirmed reduced protein expression of *ATP6V1B1* in Jag1-treated organoids as well (Figure 6F). Of note, similar to the scRNA-seq data, *AQP2* and *ATP6V1B1* copositive cells could be detected, suggesting the possible presence of transitional cells or bipotential progenitor cells. These studies suggest that kidney organoids hold promise as models to study PC and IC development and interconversion.

DISCUSSION

Three-dimensional (3D) kidney organoids differentiated from PSCs recapitulate many multicellular and anatomical hallmarks of human kidney, providing an accessible experimental platform to model human organogenesis, disease, and drug testing (Rossi et al., 2018). Two challenges that must be overcome to more fully realize the potential of kidney organoids include improving cell maturation and functional assessment rather than observational characterization. Based on the original observation that combining separately induced mouse metanephric mesenchyme and UB recapitulates branching morphogenesis (Taguchi and Nishinakamura, 2017), and the more recent demonstration by Tsujimoto et al. (2020), we have developed a methodology to apply this approach to hPSCs. This results in collecting duct being interconnected to more proximal nephron segments. We also report that aldosterone and AVP drive maturation of PCs and ICs, including the ability to model AVP-induced AQP2 translocation and water transport. Hormone treatment did not induce collecting duct from Takasato protocol organoids, but this may not be a generalizable result because of lab-to-lab variations in the organoid differentiation even from the same protocol.

The presence of collecting duct with improved maturation may have important applications. We establish the feasibility of studying AQP2 trafficking in human PCs, for example. While well-characterized cell culture models for studying vasopressin-mediated AQP2 biology exist, these do not recapitulate the 3D collecting duct environment or include adjacent ICs and whether these factors might reveal unappreciated aspects of this pathway is unknown (Cheung et al., 2017; Rice et al., 2015). The emergence of ICs with this protocol also provides an opportunity to study collecting duct plasticity. Park et al. (2018) recently showed that PCs and ICs interconvert and that this process is regulated by Notch signaling (Park et al., 2018). We provide proof of principle that this process can be modeled since Notch pathway activation increased the ratio of PCs to ICs. Organoids have already been used to model polycystic kidney disease (PKD) (Cruz et al., 2017; Freedman et al., 2015). In autosomal dominant PKD, cysts predominantly arise from the collecting duct, and the only approved drug to treat PKD is tolvaptan, which inhibits the vasopressin receptor that is expressed on PCs (Grantham et al., 1987; Torres et al., 2012). The presence of more mature collecting duct therefore offers a chance to study cystogenesis in the most relevant cell type.

Our modified protocol also allowed more faithful injury responses, since cisplatin could induce both *HAVCR1* and *NGAL* protein in proximal and distal tubule, respectively. The emergence of urothelial cell clusters also suggests the possibility that future protocol enhancements could result in the generation a full collecting system, potentially including a ureter. At present, how to "plumb in" differentiated organoids to ureteral tissue remains a major hurdle for the field. By contrast, we observed only occasional endothelial cells, and this is a limitation of the current protocol. Whether shear stress might induce the formation of a vascular network with organoids differentiated using this protocol remains an open question (Homan et al., 2019).

STAR★METHODS

Detailed methods are provided in the online version of this paper and include the following:

- KEY RESOURCES TABLE
- RESOURCE AVAILABILITY
  - Lead Contact
  - Materials Availability
  - Data and Code Availability
- EXPERIMENTAL MODEL AND SUBJECT DETAILS
  - Human iPSC or ESC Culture
- METHOD DETAILS
  - PIM lineage induction from human iPSCs or ESCs
  - AIM lineage induction from human iPSCs or ESCs
  - Generating kidney organoids by combining AIM and PIM
  - Single cell RNA-seq
  - Immunofluorescence
  - Whole-mount immunohistochemistry
  - Scanning electron microscopy (SEM) imaging
  - Real Time PCR Experiments
  - Western blot
  - Principal Cell isolation
  - AQP2 trafficking assay
  - Quantitation of AQP2 insertion
  - Jag1 experiment
  - Single cell RNA-seq data analysis
- QUANTIFICATION AND STATISTICAL ANALYSIS
  - Statistical analysis

SUPPLEMENTAL INFORMATION

Supplemental Information can be found online at https://doi.org/10.1016/j.celrep.2020.108514.

ACKNOWLEDGMENTS

This work was supported by NIH/NIDDK DK103740 and DK107374, by an Established Investigator Award of the American Heart Association, and by grant 173970 from the Chan Zuckerberg Initiative (all to B.D.H.). K.U. was supported by JSPS Postdoctoral Fellowships for Research Abroad.

AUTHOR CONTRIBUTIONS

K.U. designed and carried out experiments, analyzed results, and approved the manuscript. H.W. designed and carried out the scRNA-seq experiments,

analyzed results, and contributed to the writing of the manuscript. Y.Y. designed and carried out experiments, analyzed results, and approved the manuscript. B.D.H. designed experiments, analyzed results, and wrote the manuscript.

DECLARATION OF INTERESTS

The authors declare no competing interests.

Received: May 20, 2019
Revised: July 17, 2019
Accepted: November 19, 2020
Published: December 15, 2020

REFERENCES

Bakken, T.E., Hodge, R.D., Miller, J.A., Yao, Z., Nguyen, T.N., Aevermann, B., Barkan, E., Bertagnolli, D., Casper, T., Dee, N., et al. (2018). Single-nucleus and single-cell transcriptomes compared in matched cortical cell types. PLoS ONE *13*, e0209648.

Becht, E., McInnes, L., Healy, J., Dutertre, C.A., Kwok, I.W.H., Ng, L.G., Ginhoux, F., and Newell, E.W. (2018). Dimensionality reduction for visualizing single-cell data using UMAP. Nat. Biotechnol. *37*. https://doi.org/10.1038/nbt.4314.

Blomqvist, S.R., Vidarsson, H., Fitzgerald, S., Johansson, B.R., Ollerstam, A., Brown, R., Persson, A.E., Bergström G, Gö., and Enerbäck, S. (2004). Distal renal tubular acidosis in mice that lack the forkhead transcription factor Foxi1. J. Clin. Invest. *113*, 1560–1570.

Butler, A., Hoffman, P., Smibert, P., Papalexi, E., and Satija, R. (2018). Integrating single-cell transcriptomic data across different conditions, technologies, and species. Nat. Biotechnol. *36*, 411–420.

Cheung, P.W., Ueberdiek, L., Day, J., Bouley, R., and Brown, D. (2017). Protein phosphatase 2C is responsible for VP-induced dephosphorylation of AQP2 serine 261. Am. J. Physiol. Renal Physiol. *313*, F404–F413.

Cruz, N.M., Song, X., Czerniecki, S.M., Gulieva, R.E., Churchill, A.J., Kim, Y.K., Winston, K., Tran, L.M., Diaz, M.A., Fu, H., et al. (2017). Organoid cystogenesis reveals a critical role of microenvironment in human polycystic kidney disease. Nat. Mater. *16*, 1112–1119.

Czerniecki, S.M., Cruz, N.M., Harder, J.L., Menon, R., Annis, J., Otto, E.A., Gulieva, R.E., Islas, L.V., Kim, Y.K., Tran, L.M., et al. (2018). High-Throughput Screening Enhances Kidney Organoid Differentiation from Human Pluripotent Stem Cells and Enables Automated Multidimensional Phenotyping. Cell Stem Cell *22*, 929–940.e924.

Drake, K.A., Adam, M., Mahoney, R., and Potter, S.S. (2018). Disruption of Hox9,10,11 function results in cellular level lineage infidelity in the kidney. Sci. Rep. *8*, 6306.

Ecelbarger, C.A., Nielsen, S., Olson, B.R., Murase, T., Baker, E.A., Knepper, M.A., and Verbalis, J.G. (1997). Role of renal aquaporins in escape from vasopressin-induced antidiuresis in rat. J. Clin. Invest. *99*, 1852–1863.

Eldred, K.C., Hadyniak, S.E., Hussey, K.A., Brenerman, B., Zhang, P.W., Chamling, X., Sluch, V.M., Welsbie, D.S., Hattar, S., Taylor, J., et al. (2018). Thyroid hormone signaling specifies cone subtypes in human retinal organoids. Science *362*, eaau6348.

Fischer, E.A., Verpont, M.C., Garrett-Sinha, L.A., Ronco, P.M., and Rossert, J.A. (2001). Klf6 is a zinc finger protein expressed in a cell-specific manner during kidney development. J. Am. Soc. Nephrol. *12*, 726–735.

Freedman, B.S., Brooks, C.R., Lam, A.Q., Fu, H., Morizane, R., Agrawal, V., Saad, A.F., Li, M.K., Hughes, M.R., Werff, R.V., et al. (2015). Modelling kidney disease with CRISPR-mutant kidney organoids derived from human pluripotent epiblast spheroids. Nat. Commun. *6*, 8715.

Grantham, J.J., Geiser, J.L., and Evan, A.P. (1987). Cyst formation and growth in autosomal dominant polycystic kidney disease. Kidney Int. *31*, 1145–1152.

Gubler, M.C. (2014). Renal tubular dysgenesis. Pediatr. Nephrol. *29*, 51–59.

Han, X., Zhou, Z., Fei, L., Sun, H., Wang, R., Chen, Y., Chen, H., Wang, J., Tang, H., Ge, W., et al. (2020). Construction of a human cell landscape at single-cell level. Nature *581*, 303–309.

Harding, S.D., Armit, C., Armstrong, J., Brennan, J., Cheng, Y., Haggarty, B., Houghton, D., Lloyd-MacGilp, S., Pi, X., Roochun, Y., et al. (2011). The GUDMAP database–an online resource for genitourinary research. Development *138*, 2845–2853.

Higgins, J.W., Chambon, A., Bishard, K., Hartung, A., Arndt, D., Brugnano, J., Er, P.X., Lawlor, K.T., Vanslambrouck, J.M., Wilson, S., et al. (2018). Bioprinted pluripotent stem cell-derived kidney organoids provide opportunities for high content screening. bioRxiv. https://doi.org/10.1101/505396.

Hochane, M., van den Berg, P.R., Fan, X., Bérenger-Currias, N., Adegeest, E., Bialecka, M., Nieveen, M., Menschaart, M., Chuva de Sousa Lopes, S.M., and Semrau, S. (2019). Single-cell transcriptomics reveals gene expression dynamics of human fetal kidney development. PLoS Biol. *17*, e3000152.

Homan, K.A., Gupta, N., Kroll, K.T., Kolesky, D.B., Skylar-Scott, M., Miyoshi, T., Mau, D., Valerius, M.T., Ferrante, T., Bonventre, J.V., et al. (2019). Flow-enhanced vascularization and maturation of kidney organoids in vitro. Nat. Methods *16*, 255–262.

Howden, S.E., Vanslambrouck, J.M., Wilson, S.B., Tan, K.S., and Little, M.H. (2019). Reporter-based fate mapping in human kidney organoids confirms nephron lineage relationships and reveals synchronous nephron formation. EMBO Rep. *20*, e47483.

Ichimura, T., Bonventre, J.V., Bailly, V., Wei, H., Hession, C.A., Cate, R.L., and Sanicola, M. (1998). Kidney injury molecule-1 (KIM-1), a putative epithelial cell adhesion molecule containing a novel immunoglobulin domain, is up-regulated in renal cells after injury. J. Biol. Chem. *273*, 4135–4142.

Jeong, H.W., Jeon, U.S., Koo, B.K., Kim, W.Y., Im, S.K., Shin, J., Cho, Y., Kim, J., and Kong, Y.Y. (2009). Inactivation of Notch signaling in the renal collecting duct causes nephrogenic diabetes insipidus in mice. J. Clin. Invest. *119*, 3290–3300.

Klingberg, A., Hasenberg, A., Ludwig-Portugall, I., Medyukhina, A., Männ, L., Brenzel, A., Engel, D.R., Figge, M.T., Kurts, C., and Gunzer, M. (2017). Fully Automated Evaluation of Total Glomerular Number and Capillary Tuft Size in Nephritic Kidneys Using Lightsheet Microscopy. J. Am. Soc. Nephrol. *28*, 452–459.

Kobayashi, A., Kwan, K.M., Carroll, T.J., McMahon, A.P., Mendelsohn, C.L., and Behringer, R.R. (2005). Distinct and sequential tissue-specific activities of the LIM-class homeobox gene Lim1 for tubular morphogenesis during kidney development. Development *132*, 2809–2823.

Korsunsky, I., Fan, J., Slowikowski, K., Zhang, F., Wei, K., Baglaenko, Y., Brenner, M., Loh, P.-R., and Raychaudhuri, S. (2019). Fast, sensitive, and accurate integration of single cell data with Harmony. Nat. Methods *16*, 1289–1296.

Mae, S.I., Ryosaka, M., Toyoda, T., Matsuse, K., Oshima, Y., Tsujimoto, H., Okumura, S., Shibasaki, A., and Osafune, K. (2018). Generation of branching ureteric bud tissues from human pluripotent stem cells. Biochem. Biophys. Res. Commun. *495*, 954–961.

McGinnis, C.S., Murrow, L.M., and Gartner, Z.J. (2019). DoubletFinder: Doublet Detection in Single-Cell RNA Sequencing Data Using Artificial Nearest Neighbors. Cell Syst. *8*, 329–337.e324.

Mendelsohn, C. (2009). Using mouse models to understand normal and abnormal urogenital tract development. Organogenesis *5*, 306–314.

Menon, R., Otto, E.A., Kokoruda, A., Zhou, J., Zhang, Z., Yoon, E., Chen, Y.C., Troyanskaya, O., Spence, J.R., Kretzler, M., and Cebrián, C. (2018). Single-cell analysis of progenitor cell dynamics and lineage specification in the human fetal kidney. Development *145*, dev164038.

Morizane, R., Lam, A.Q., Freedman, B.S., Kishi, S., Valerius, M.T., and Bonventre, J.V. (2015). Nephron organoids derived from human pluripotent stem cells model kidney development and injury. Nat. Biotechnol. *33*, 1193–1200.

Narlis, M., Grote, D., Gaitan, Y., Boualia, S.K., and Bouchard, M. (2007). Pax2 and pax8 regulate branching morphogenesis and nephron differentiation in the developing kidney. J. Am. Soc. Nephrol. *18*, 1121–1129.

Nielsen, S., DiGiovanni, S.R., Christensen, E.I., Knepper, M.A., and Harris, H.W. (1993). Cellular and subcellular immunolocalization of vasopressin-regulated water channel in rat kidney. Proc. Natl. Acad. Sci. USA *90*, 11663–11667.

Paragas, N., Qiu, A., Zhang, Q., Samstein, B., Deng, S.X., Schmidt-Ott, K.M., Viltard, M., Yu, W., Forster, C.S., Gong, G., et al. (2011). The Ngal reporter mouse detects the response of the kidney to injury in real time. Nat. Med. *17*, 216–222.

Park, J., Shrestha, R., Qiu, C., Kondo, A., Huang, S., Werth, M., Li, M., Barasch, J., and Suszták, K. (2018). Single-cell transcriptomics of the mouse kidney reveals potential cellular targets of kidney disease. Science *360*, 758–763.

Pearce, D., Soundararajan, R., Trimpert, C., Kashlan, O.B., Deen, P.M., and Kohan, D.E. (2015). Collecting duct principal cell transport processes and their regulation. Clin. J. Am. Soc. Nephrol. *10*, 135–146.

Phipson, B., Er, P.X., Combes, A.N., Forbes, T.A., Howden, S.E., Zappia, L., Yen, H.J., Lawlor, K.T., Hale, L.J., Sun, J., et al. (2019). Evaluation of variability in human kidney organoids. Nat. Methods *16*, 79–87.

Qiu, X., Hill, A., Packer, J., Lin, D., Ma, Y.A., and Trapnell, C. (2017). Single-cell mRNA quantification and differential analysis with Census. Nat. Methods *14*, 309–315.

Rice, W.L., Li, W., Mamuya, F., McKee, M., Păunescu, T.G., and Lu, H.A. (2015). Polarized Trafficking of AQP2 Revealed in Three Dimensional Epithelial Culture. PLoS ONE *10*, e0131719.

Rossi, G., Manfrin, A., and Lutolf, M.P. (2018). Progress and potential in organoid research. Nat. Rev. Genet. *19*, 671–687.

Subramanian, A., Sidhom, E.-H., Emani, M., Vernon, K., Sahakian, N., Zhou, Y., Kost-Alimova, M., Slyper, M., Waldman, J., Dionne, D., et al. (2019). Single cell census of human kidney organoids shows reproducibility and diminished off-target cells after transplantation. Nat. Commun. *10*, 5462.

Taguchi, A., and Nishinakamura, R. (2017). Higher-Order Kidney Organogenesis from Pluripotent Stem Cells. Cell Stem Cell *21*, 730–746.e736.

Taguchi, A., Kaku, Y., Ohmori, T., Sharmin, S., Ogawa, M., Sasaki, H., and Nishinakamura, R. (2014). Redefining the in vivo origin of metanephric nephron progenitors enables generation of complex kidney structures from pluripotent stem cells. Cell Stem Cell *14*, 53–67.

Takasato, M., Er, P.X., Becroft, M., Vanslambrouck, J.M., Stanley, E.G., Elefanty, A.G., and Little, M.H. (2014). Directing human embryonic stem cell differentiation towards a renal lineage generates a self-organizing kidney. Nat. Cell Biol. *16*, 118–126.

Takasato, M., Er, P.X., Chiu, H.S., Maier, B., Baillie, G.J., Ferguson, C., Parton, R.G., Wolvetang, E.J., Roost, M.S., Chuva de Sousa Lopes, S.M., and Little, M.H. (2015). Kidney organoids from human iPS cells contain multiple lineages and model human nephrogenesis. Nature *526*, 564–568.

Takasato, M., Er, P.X., Chiu, H.S., and Little, M.H. (2016). Generation of kidney organoids from human pluripotent stem cells. Nat. Protoc. *11*, 1681–1692.

Torres, V.E., Chapman, A.B., Devuyst, O., Gansevoort, R.T., Grantham, J.J., Higashihara, E., Perrone, R.D., Krasa, H.B., Ouyang, J., and Czerwiec, F.S.; TEMPO 3:4 Trial Investigators (2012). Tolvaptan in patients with autosomal dominant polycystic kidney disease. N. Engl. J. Med. *367*, 2407–2418.

Tsujimoto, H., Kasahara, T., Sueta, S.I., Araoka, T., Sakamoto, S., Okada, C., Mae, S.I., Nakajima, T., Okamoto, N., Taura, D., et al. (2020). A Modular Differentiation System Maps Multiple Human Kidney Lineages from Pluripotent Stem Cells. Cell Rep. *31*, 107476.

van den Berg, C.W., Ritsma, L., Avramut, M.C., Wiersma, L.E., van den Berg, B.M., Leuning, D.G., Lievers, E., Koning, M., Vanslambrouck, J.M., Koster, A.J., et al. (2018). Renal Subcapsular Transplantation of PSC-Derived Kidney Organoids Induces Neo-vasculogenesis and Significant Glomerular and Tubular Maturation In Vivo. Stem Cell Reports *10*, 751–765.

Werth, M., Schmidt-Ott, K.M., Leete, T., Qiu, A., Hinze, C., Viltard, M., Paragas, N., Shawber, C.J., Yu, W., Lee, P., et al. (2017). Transcription factor *TFCP2L1* patterns cells in the mouse kidney collecting ducts. eLife *6*, e24265.

Wu, H., Uchimura, K., Donnelly, E.L., Kirita, Y., Morris, S.A., and Humphreys, B.D. (2018). Comparative Analysis and Refinement of Human PSC-Derived Kidney Organoid Differentiation with Single-Cell Transcriptomics. Cell Stem Cell *23*, 869–881.e868.

Wu, H., Kirita, Y., Donnelly, E.L., and Humphreys, B.D. (2019). Advantages of Single-Nucleus over Single-Cell RNA Sequencing of Adult Kidney: Rare Cell Types and Novel Cell States Revealed in Fibrosis. J. Am. Soc. Nephrol. *30*, 23–32.

Xia, Y., Sancho-Martinez, I., Nivet, E., Rodriguez Esteban, C., Campistol, J.M., and Izpisua Belmonte, J.C. (2014). The generation of kidney organoids by differentiation of human pluripotent cells to ureteric bud progenitor-like cells. Nat. Protoc. *9*, 2693–2704.

STAR★METHODS

KEY RESOURCES TABLE

REAGENT or RESOURCE	SOURCE	IDENTIFIER
Antibodies		
anti-AQP2	Novus Biologicals	Cat#NB110-74682; RRID: AB_1107363
anti-AQP2	Santa Cruz Biothechnology	Cat#SC-9882; RRID: AB_2289903
Rhodamine labeled DBA	Vector Labs	Cat#RL-1032; RRID: AB_2336396
anti-ECAD	Abcam	Cat#ab11512; RRID: AB_298118
anti-WT1	Santa Cruz Biothechnology	Cat#SC-7385; RRID: AB_628448
biotinylated LTL	Vector Labs	Cat#B-1325; RRID: AB_2336558
anti-MEIS1	Active Motif	Cat#39795; RRID: AB_2750570
anti-PDGFRB	Abcam	Cat#ab32570; RRID: AB_777165
anti-ATP6V1B1	Santa Cruz Biothechnology	Cat#SC-55544; RRID: AB_831844
anti-ATP6V1B1	Abcam	Cat#ab76020; RRID: AB_1310695
anti-SLC12A1	Abcam	Cat#ab171747; RRID: AB_2802126
anti-CD31	R&D Systems	Cat#bba7; RRID: AB_356960
anti-NPHS1	R&D Systems	Cat#AF4269; RRID: AB_2154851
anti-CK8	Abcam	Cat#ab9023; RRID: AB_306948
anti-Na/K/ATPase	Abcam	Cat#ab76020; RRID: AB_1310695
anti-HAVCR1	R&D Systems	Cat#AF1750; RRID: AB_2116561
anti-SOX9	Abcam	Cat#ab185230; RRID: AB_2715497
anti-NGAL	Abcam	Cat#ab23477; RRID: AB_447460
anti-KRT7	Abcam	Cat#ab9021; RRID: AB_306947
anti-UPK2	Novus Biologicals	Cat#NBP2-33389
Secondary antibodies included FITC-, Cy3, or Cy5-conjugated	Jackson ImmunoResearch	Cat#711-095-152; RRID: AB_2315776, Cat#712-095-153; RRID: AB_2340652, Cat#715-165-151; RRID: AB_2315777, Cat#713-165-147; RRID: AB_2315778, Cat#016-600-084; RRID: AB_2341101, Cat#703-165-155; RRID: AB_2340363
Secondary antibodies included AlexaFlour488-, or AlexaFlour568-conjugated	Thermo Fisher Scientific	Cat#A21206; RRID: AB_2535792, Cat#A21202; RRID: AB_141607, Cat#A11057; RRID: AB_142581
anti-HOXD11	Millipore Sigma	Cat#SAB1403944; RRID: AB_10739483
anti-GATA3	R&D Systems	Cat#AF2605; RRID: AB_2108571
Chemicals, Peptides, and Recombinant Proteins		
StemFlex Medium	Thermo Fisher Scientific	Cat#A3349401
Stemdiff APEL2 Medium	STEMCELL Technologies	Cat#05275
Protein Free Hybridoma Medium II	Thermo Fisher Scientific	Cat#12040077
Matrigel hESC-Qualified Matrix	Corning	Cat#354277
CHIR99021	Tocris Bioscience	Cat#4423
FGF9	R&D Systems	Cat#273-F9-025/CF
Heparin	Millipore Sigma	Cat#H4784
Activin A	R&D Systems	Cat#338-AC
Bmp4	R&D Systems	Cat#314-BP
Retinoic acid	Millipore Sigma	Cat#R2625
LDN193189	Axon Medchem	Cat#Azon1509
GDNF	R&D Systems	Cat#212-GD

(*Continued on next page*)

Continued

REAGENT or RESOURCE	SOURCE	IDENTIFIER
EGF	Thermo Fisher Scientific	Cat#PHG0311
Aldosterone	Millipore Sigma	Cat#A9477
AVP	Millipore Sigma	Cat#V9879
K-252a	Millipore Sigma	Cat#K1639
ReLeSR	STEMCELL Technologies	Cat#05872
0.25% Trypsin-EDTA	Thermo Fisher Scientific	Cat#25200-114
Antibiotic-Antimycotic	Thermo Fisher Scientific	Cat#15240-062
Cisplatin	Millipore Sigma	Cat#P4394
Forskorin	Selleck Chemicals	Cat#S2449
Phalloidin-FITC	Millipore Sigma	Cat#P5282
DAPI (4',6'- diamidino-2-phenylindole)	Thermo Fisher Scientific	Cat#D1306
Critical Commercial Assays		
Chromium Single Cell 5¿ Library & Gel Bead Kit	10x Genomics	Cat#PN-1000006
Deposited Data		
Kidney organoid scRNA-seq	This study	GEO:GSE131086
Experimental Models: Cell Lines		
Human iPSCs: BJFF.6 line	GEiC	N/A
Human ESCs: H9 line	GEiC	N/A
Oligonucleotides		
All qPCR oligos	This study	Table S3
Software and Algorithms		
CellRanger	10x Genomics	N/A
Seurat	https://satijalab.org/seurat/	N/A
DoubletFinder	https://github.com/chris-mcginnis-ucsf/DoubletFinder	N/A
Harmony	https://github.com/immunogenomics/harmony	N/A
Monocle2	http://cole-trapnell-lab.github.io/monocle-release/docs/	N/A
scHCL	https://github.com/ggjlab/scHCL/	N/A
Other		
Fetal human kidney scRNA-seq	Hochane et al., 2019	GEO:GSE114530
Adult human kidney scRNA-seq	Wu et al., 2018	GEO:GSE118184

RESOURCE AVAILABILITY

Lead Contact

Further information and requests for resources and reagents should be directed to and will be fulfilled by the Lead Contact, Benjamin D. Humphreys (humphreysbd@wustl.edu).

Materials Availability

This study did not generate new or unique reagents.

Data and Code Availability

The accession number for the RNA sequencing data reported in this paper is NCBI GEO: GSE131086.

The human fetal and adult kidney datasets are publicly available from GEO: GSE114530 and GSE118184.

This study did not generate code.

EXPERIMENTAL MODEL AND SUBJECT DETAILS

Human iPSC or ESC Culture

All experiments utilized the BJFF6 human iPSC and H9 human ESC lines (Washington University Genome Engineering and iPSC Core). These lines are confirmed to be karyotypically normal and maintained in 6-well plates coated with matrigel (Corning) in Stem Flex medium (Thermo Fisher Scientific). These cells were dissociated using ReLeSR (STEMCELL Technologies), confirmed to be mycoplasma free and maintained below passage 50.

METHOD DETAILS

PIM lineage induction from human iPSCs or ESCs

Until Day 7, MM lineage cells were induced following the Takasato protocol (Takasato et al., 2016). Briefly, pluripotent stem cells were treated with CHIR (8 μM, Tocris Bioscience) in basal medium - APEL 2 (STEMCELL Technologies) supplemented with 5% Protein Free Hybridoma Medium II (PFHMII, GIBCO) for 4 days, followed by FGF9 (200 ng/mL, R&D Systems) and heparin (1 μg/mL, Sigma-Aldrich) for another 3 days.

AIM lineage induction from human iPSCs or ESCs

The differentiation started with CHIR (8 uM) treatment for one day, followed by treatment with CHIR (8 μM), Activin A (10 ng/mL, R&D Systems), and BMP4 (1 ng/mL, R&D Systems) for two days, followed by FGF9 (200 ng/mL), heparin (1 μg/mL, Sigma-Aldrich), Activin A (1 ng/mL), RA (100 nM, Sigma-Aldrich), and LDN193189 (100 nM, Axon Medchem) for 4 days with the exception that LDN193189 was reduced to 30 nM after two days.

Generating kidney organoids by combining AIM and PIM

At day 7, AIM and PIM lineage cells were collected and dissociated into single cell suspension using 0.25% Trypsin-EDTA (Thermo Fisher Scientific). 0.5×10^6 cells were mixed at ratios ranging from 1:3 to 3:1 and spun down at 400 g for 3 min to form a pellet. The pellets were transferred onto a trans-well membrane and incubated with CHIR (5 μM) for 1 hour, then cultured with FGF9 (200 ng/mL), heparin (1 μg/mL), RA (100 nM), GDNF (10 ng/mL, R&D Systems), and EGF (10 ng/mL, Thermo Fisher Scientific) for 5 days. For the next 13 days, the organoids were cultured in basal medium supplemented with aldosterone (10 nM, Sigma-Aldrich), AVP (10 nM, Sigma-Aldrich), and K252a (100 nM, Sigma-Aldrich) changed every other day.

Single cell RNA-seq

Organoids from Uchimura and Takasato protocols were harvested at day 26 and dissociated into single cells using TrypLE. Cells were counted on hemocytometers (InCYTO C-chip) and partitioned into each droplet with a barcoded gel bead using the 10x Chromium instrument (10x Genomics, Pleasanton, CA). Single cell was lysed and RNAs were reverse transcribed into cDNA within each droplet. After breaking the emulsion, cDNAs were amplified and fragmented followed by the addition of Illumina adapters using the Chromium Single Cell 5¿ Library & Gel Bead Kit. Samples were indexed and sequenced on the S4 flow cell of NovaSeq 6000 (Illumina).

Immunofluorescence

Organoids were fixed in 4% paraformaldehyde (Electron Microscopy Services), cryoprotected in 30% sucrose solution overnight and embedded in optimum cutting temperature (OCT) compound (Tissue Tek). Organoids were cryosectioned at 6 μm thickness and mounted on Superfrost slides (Thermo Fisher Scientific). Sections were washed with PBS (3 times, 5 minutes each), then blocked with 1% BSA (Sigma-Aldrich) in PBS, permeabilized with 0.1% Triton X-100 (Sigma-Aldrich) in PBS and then stained with primary antibodies (see Key Resources Table) at 4°C overnight. Next, the sections were stained with secondary antibodies (see Key Resources Table) for 60 min at room temperature. Then, sections were stained with DAPI (4′,6′- diamidino-2-phenylindole) and mounted in Prolong Gold (Life Technologies). Images were obtained by confocal microscopy (Nikon C2+ Eclipse; Nikon, Melville, NY).

Whole-mount immunohistochemistry

Organoids were fixed in 4% paraformaldehyde in PBS for 60 min, washed with 0.1% Triton X-100 in PBS three times, and blocked in PBS containing 1% BSA, 0.3% Triton X-100, and 0.2% dry skim milk (LabScientific) for 1 h twice. The tissues were incubated for two days with primary antibodies (see Key Resources Table) on a rocking shaker at 4 C, washed with 0.3%Triton X-100 in PBS for 1 h three times, and incubated with secondary antibodies overnight (see Key Resources Table). After immunostaining, the organoids were cleared exactly as described (Klingberg et al., 2017). The specimens were dehydrated with 50% and 70% ethanol in H2O, 100% ethanol twice, and ethyl cinnamate. 3D fluorescence images were captured by confocal microscopy and reconstructed by software (Nikon NIS-Elements Advanced Research).

Scanning electron microscopy (SEM) imaging

Immediately before fixation, make a solution of 2.5% glutaraldehyde + 2% paraformaldehyde in 0.15M cacodylate buffer (final concentrations) and warm to 37þC. Gently pellet organoids in a 1.5mL eppendorf tube, remove cell media, re-suspend in warm fixative, and return to the incubator for 5min. After 5 min, remove samples from the incubator and continue to fix for one hour at room temperature. Gently pellet, remove fixative, and rinse in 0.15M cacodylate buffer for 5 minutes. After the fixation, the images were captured by SEM (Zeiss Merlin FE-SEM).

Real Time PCR Experiments

RNA from whole organoids was extracted using the RNeasy Mini Kit (QIAGEN) and 600 ng of total RNA was reverse transcribed with iScript (BioRad). Quantitative polymerase chain reactions were carried out with iQ-SYBR Green supermix (BioRad) and the BioRad CFX96 Real Time System with the C1000 Touch Thermal Cycler. Cycling conditions were 95°C for 3 minutes then 40 cycles of 95°C for 15 s and 60°C for 1 minute, followed by one cycle of 95°C for 10 s. Glyceraldehyde-3-phosphate dehydrogenase (GAPDH) was used as a housekeeping gene. Data was analyzed using the $2^{-\Delta\Delta ct}$ method. Primer sequences are listed in Key Resources Table.

Western blot

The organoids were washed with 1 × PBS and lysates prepared in RIPA buffer with protease inhibitors (Roche). Protein concentration was measured using the BCA assay (Thermo Fisher). Using 10% polyacrylamide gel, 10–20 μg of protein was separated by SDS electrophoresis and transferred to an Immobilon PVDF membrane (Millipore). Membrane was blocked with 5% milk in TBST and probed overnight at 4°C with anti-NGAL (Abcam, #ab125075) antibody. After washing the membrane with TBST, it was incubated for 1 hour at room temperature with HRP-conjugated secondary antibody (Dako). The membrane was developed using the ECL Detection System (GE Healthcare).

Principal Cell isolation

On day 26, the organoids were harvested and dissociated by incubation in 0.25% trypsin/EDTA for 10 min at 37 C. The single-cell suspension was incubated with FITC-conjugated DBA (FL-1031; Vector Laboratories), and washed twice in FACS buffer. The DBA+ (FITC channel) and DBA- populations were flow-sorted (Aria II; BD Biosciences).

AQP2 trafficking assay

Isolated PCs were seeded into Matrigel coated glass chamber slides and cultured with basal medium containing 10 nM Aldosterone and 10 nM AVP for 24 hours. After 2 hours incubation without Aldosterone or AVP, the cells were stimulated with forskolin (10 μM for 20 minutes). The cells were fixed with paraformaldehyde (4%), and AQP2 was detected using rabbit anti-AQP2 antibody and Cy3-coupled secondary antirabbit antibody. Nuclei were stained with DAPI, and F-actin was labeled with FITC-phalloidin.

Quantitation of AQP2 insertion

For assessment of AQP2 insertion, we measured the distance from the apical membrane to the peak AQP2 fluorescence and divided this by the distance from the apical membrane to the basolateral membrame. All distances were measured using ImageJ.

Jag1 experiment

Organoids from Uchimura protocol were exposed to Jag1 (100 ng/mL R&D Systems) from Day 19 to Day 26. After the Jag1 stimulation, the organoids were harvested for immunofluorescences and real time PCR.

Single cell RNA-seq data analysis

1. Pre-processing of the 10x sequencing reads

Raw reads were demultiplexed using the command ''cellranger mkfastq'' from the CellRanger toolkit (version 3.0). Read alignment, barcode identification and UMI quantification were completed using the command ''cellranger count.'' The output gene-level UMI count matrix for each dataset was used for downstream analysis.

2. Single cell clustering and cell type annotation

Seurat R package (v2.4)(Butler et al., 2018) was used to identify the cell types present in different organoid differentiation protocols. In brief, we first filtered out the low quality cells if their total number of genes detected were less than 1000 or more than 4000. We also removed the cells if their mitochondrial gene content was greater than 15%. After QC, we performed data normalization, data scaling and dimensionality reduction using the internal functions in Seurat. Graph-based clustering was performed after running the non-linear dimensional reduction algorithm Uniform Manifold Approximation and Projection (UMAP) (Becht et al., 2018). After applying this clustering approach to each individual dataset, we detected and removed the doublets using the DoubletFinder package (McGinnis et al., 2019). The 'doublet-free' dataset was then subject to a second round of clustering using the same clustering approach to identify the organoid cell types for each organoid protocol. We annotated the cell clusters based on the expression of the known cell type specific markers (after FindAllMarkers function in Seurat) and by comparing the clusters to the cell types on the published organoid datasets (Wu et al., 2018) based on their pairwise Pearson correlation.

3. Integrative analysis of organoid cell types from different protocols

We used Harmony (Korsunsky et al., 2019) to perform integrative analysis on the single cell transcriptomics for both Uchimura and Takasato's protocols. In brief, we first combined the single expression profiles for the cells from both protocols. We then performed data normalization (''NormalizeData'' function), variable gene detection (''FindVariableGenes'' function), data scaling (ScaleData function), and principal component analysis (''RunPCA'' function) using the default settings in Seurat. The two datasets were integrated using the ''RunHarmony'' function in Harmony package with the parameters: theta = 10, plot_convergence = TRUE, nclust = 50, max.iter.cluster = 20, and max.iter.harmony = 10. Clustering and UMAP were performed in Seurat using the 'harmony' data type as the dimensional reduction type (i.e., reduction.type = 'harmony'). Cells were colored code by clusters and origins to inspect the accuracy of the integration. Marker genes were identified from each aligned cell type using the FindAllMarkers function in Seurat. Protocol-based variations in cell type composition were computed based on the clustering result from this integrative analysis.

4. Cell type comparison across kidney organoids, human fetal kidney and human adult kidney

To compare the collecting duct (CD) cells from kidney organoids, fetal kidney and human adult kidney, we extracted the single cell transcriptomes for the AQP2 expressing cells from Uchimura's kidney organoid (this study), a time course fetal kidney study (Hochane et al., 2019) and our previous published adult kidney dataset (Wu et al., 2018). We then clustered the cells from different sources after the integrative analysis with Harmony. Cell fractions in each cluster were computed for each sample type. Mature and immature CD markers that passed the statistical testing were selected and visualized by dot plot (DotPlot function in Seurat). To compare the maturity of the CD cells derived from Uchimura and Takasato's organoid protocols, we selected the cells grouped into the same collecting duct cluster based on the integrative analysis described above. Since Uchimura's protocol contained a lot more collecting duct cells, this would complicate the comparison result because higher degree of cell heterogeneity tends to be found in a larger population of cells. To address this issue, we first found the best matching CD cells between the two protocols using a dropout weighted Pearson correlation approach (Bakken et al., 2018; Wu et al., 2019). With this approach, we ordered the cells from Uchimura's protocol based on the correlation score and then selected the top 594 CD cells to compare against their matched 594 CD cells from Takasato's protocol. Cell maturity measurement was based on their expression of the known mature and immature markers (Drake et al., 2018; Menon et al., 2018; Wu et al., 2018) in the CD cells from each protocol. We used the similar approach to compare the maturity of the proximal tubular cells between Uchimura and Takasato's protocols.

5. Subclustering and pseudotime analysis of the collecting duct cells

Single cell transcriptomes for the collecting duct cells were extracted from the Uchimura dataset. Cells were reclustered by Seurat and were annotated with the specific markers known for ureteric bud, principal cells (PC), intercalated cells (IC) and urothelium (Uro). To identify the genes that drive the differentiation of PC and IC, Monocle (version 2) was performed on the three UB lineage cell types (annotated with 'UB', 'PC', and 'IC'). Differential genes were computed by an internal function in the Monocle package that finds genes changing as a function of pseudotime. To validate the identity of the urothelium cluster in our dataset, we compared the single cell transcriptomes of each urothelial cell to the cell types in the Human Cell Landscape (HCL) database using a R package scHCL https://github.com/ggjlab/scHCL/. Similarity was evaluated by Pearson correlation coefficient.

QUANTIFICATION AND STATISTICAL ANALYSIS

Statistical analysis

Data are presented as mean ± SEM. ANOVA with post hoc Bonferroni correction was used for multiple group comparison. Student t test was used to compare 2 different groups. Graph-Pad Prism software, version 8.0.0 (GraphPad Software Inc) was used for statistical analysis. P value < 0.05 was considered as a statistically significant difference.

Cell Reports, Volume *33*

Supplemental Information

Human Pluripotent Stem Cell-Derived Kidney Organoids with Improved Collecting Duct Maturation and Injury Modeling

Kohei Uchimura, Haojia Wu, Yasuhiro Yoshimura, and Benjamin D. Humphreys

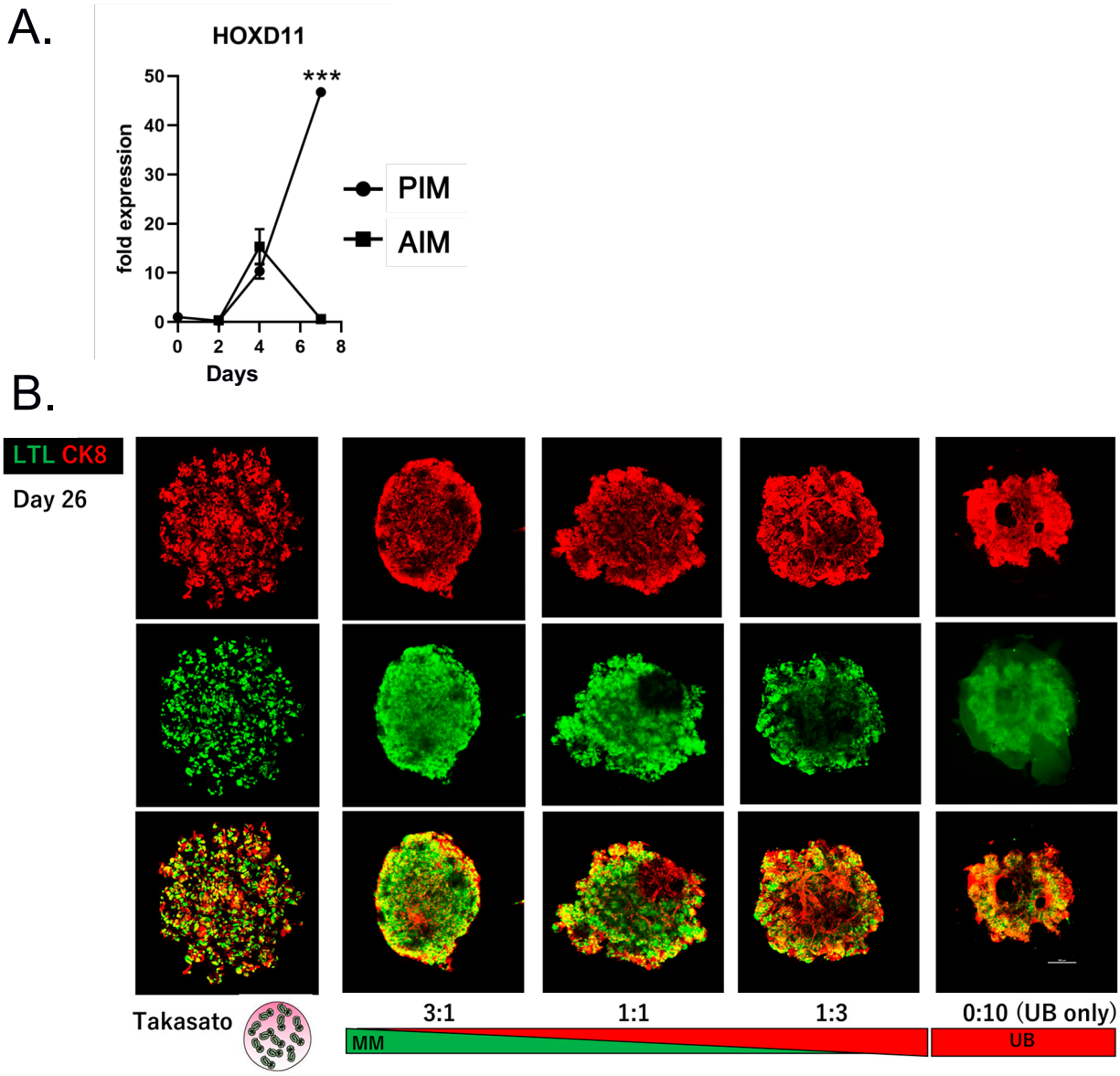

Supplemental Figure S1. HOXD11 expression in PIM vs. AIM and effect of varying ratios of PIM:AIM on CK8-positive branched structures. Related to Figure 1. A. mRNA for HOXD11 measured by qPCR at the indicated timepoints in AIM vs. PIM. HOXD11 becomes undetectable in AIM by day 7. **B.** Whole mount immunofluorescence images showing LTL and CK8 expresssion in Takasato organoids (left panel) or varying ratios of PIM:AIM with the current protocol. At ratios of 1:1 and 1:3, modest CK8 branching is seen that is abset from the 3:1 ratio. Culturing of AIM alone (right panel) results in the absence of LTL-positive proximal tubules, as expected. AIM, anterior intermediate mesoderm; PIM, posterior intermediate mesoderm. Scale bar, 500 μm.

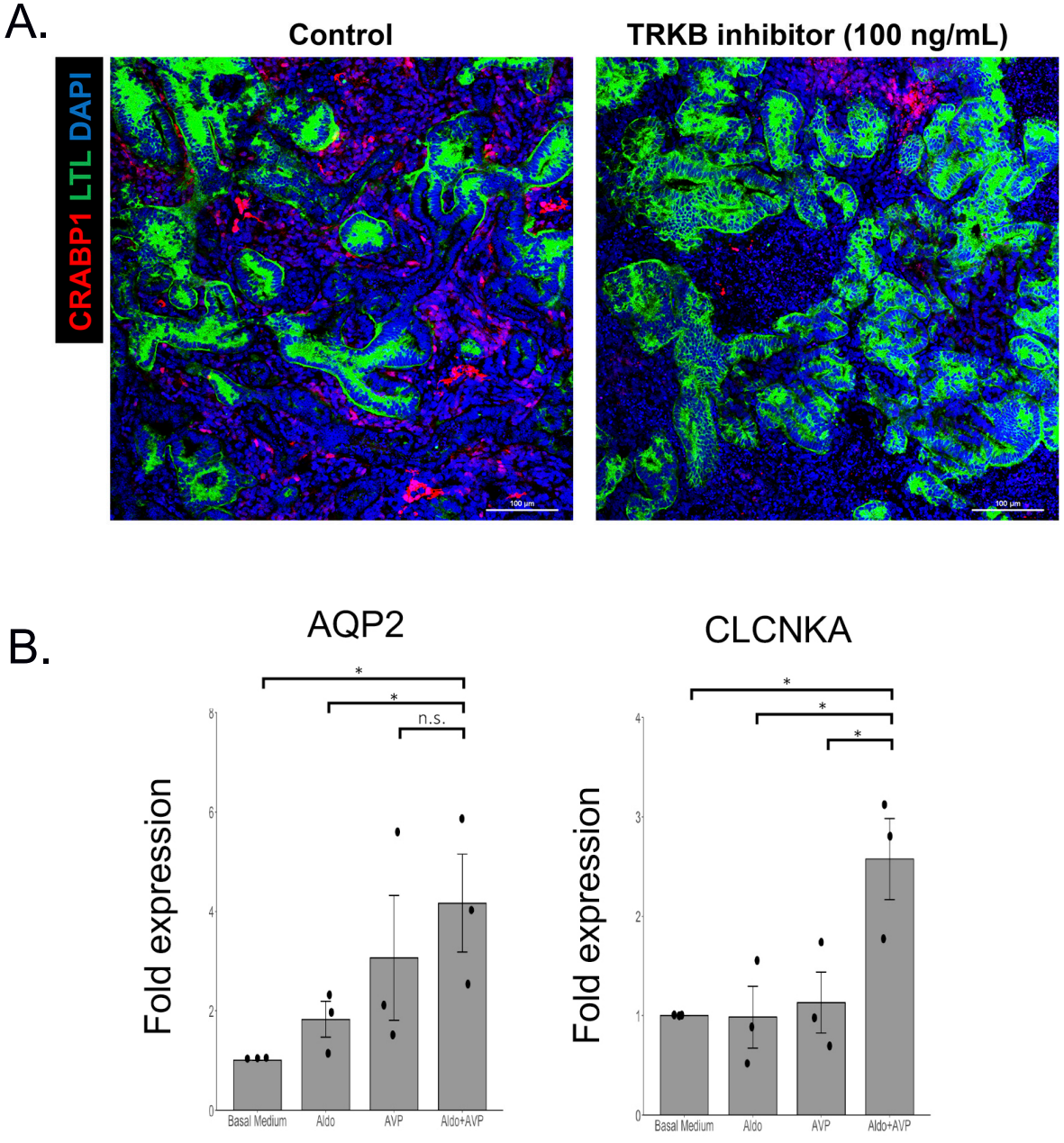

Supplemental Figure S2. Effect of TRKB inhibition on off target cells and effect of aldosterone and vasopressin alone or in combination on collecting duct marker expression. Related to Figure 1. A. Organoids were generated and treated with vehicle or 100 ng/L TRKB inhibitor K252a from day 12 – 26. LTL stains proximal tubule, and CRABP1 stains off target neuronal cells. K252a reduced CRABP1+ cells by ~80%. Representative images from n = 3 biologic replicates. Scale bar, 100 µm. **B.** Organoids were generated and treated with vehicle, 10 nM aldosterone, 10 nM AVP or the combination of aldosterone and vasopressin from days 12 – 26. mRNA levels of the principal cell marker AQP2 or the intercalated cell marker CLCNKA were measured by qPCR. Results are from n = 3 biologic replicates. *$p<0.05$.

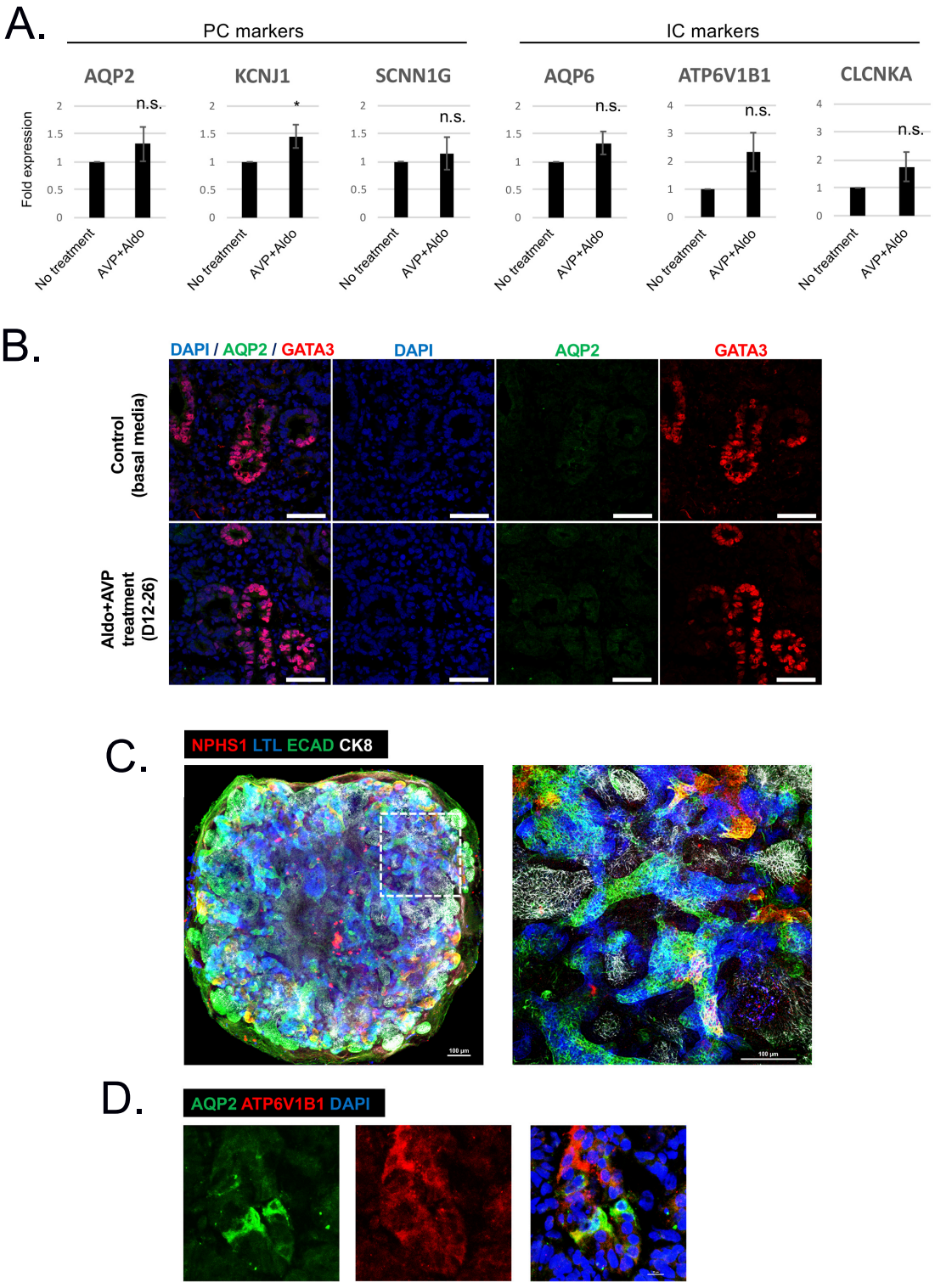

Supplemental Figure S3. Aldosterone and vasopressin do not induce principal cell or intercalated cell marker expression in Takasato organoids, kidney organoids differentiated from H9 hESCs. Related to Figure 1. A. Takasato protocol organoids were generated and treated with vehicle or 10 nM aldosterone + 10 nM AVP from days

12 – 26. mRNA levels of the principal cell and intercalated cell markers was measured by qPCR. The only marker that increased modestly with treatment is KCNJ1, which is expressed in thick ascending limb and connecting segment in addition to collecting duct. **B.** Immunofluorescence analysis of the same organoids revealed an absence of staining for the principal cell protein aquaporin-2. Results are from n = 4 biologic replicates. Scale bar, 50 μm. *$p<0.05$. **C.** Organoids were generated using the Uchimura protocol, generating all major epithelial cell types. Scale bar, 100 μm **D.** Both AQP2 positive principal cells and ATP6V1B1 positive intercalated cells were generated. Representative images from n = 3 biologic replicates. Scale bar, 10 μm.

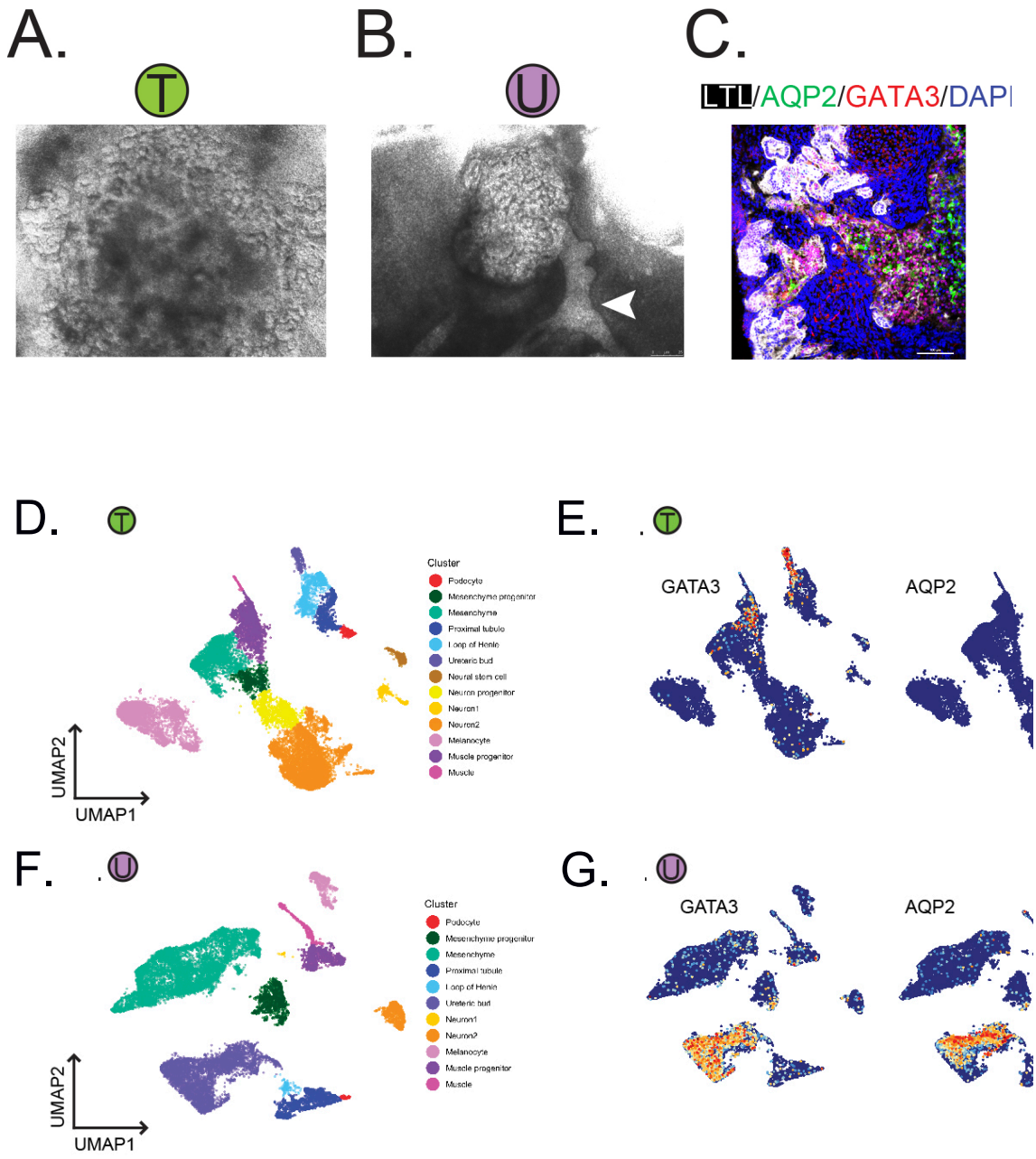

Supplemental Figure S4. Large duct-like structures from new protocol and expression of GATA3 and AQP2 between protocols. Related to Figure 2 and Figure 4. A,B. The presence of branching larger duct structures (arrowhead) are visible by brightfield in Uchimura organoids, but not in Takasato organoids. **C.** Collecting duct (GATA3+, AQP2+) is located in the central region of the organoid with proximal tubule (LTL+) on the periphery. Scale bar, 100 μm. **D.** UMAP of all cell types from Takasato protocol organoid. **E.** Expression of GATA3 and AQP2 in Takasato organoid. **F.** UMAP of all cell types from Uchimura organoid. **G.** Expression of GATA3 and AQP2 in Uchimura organoid.

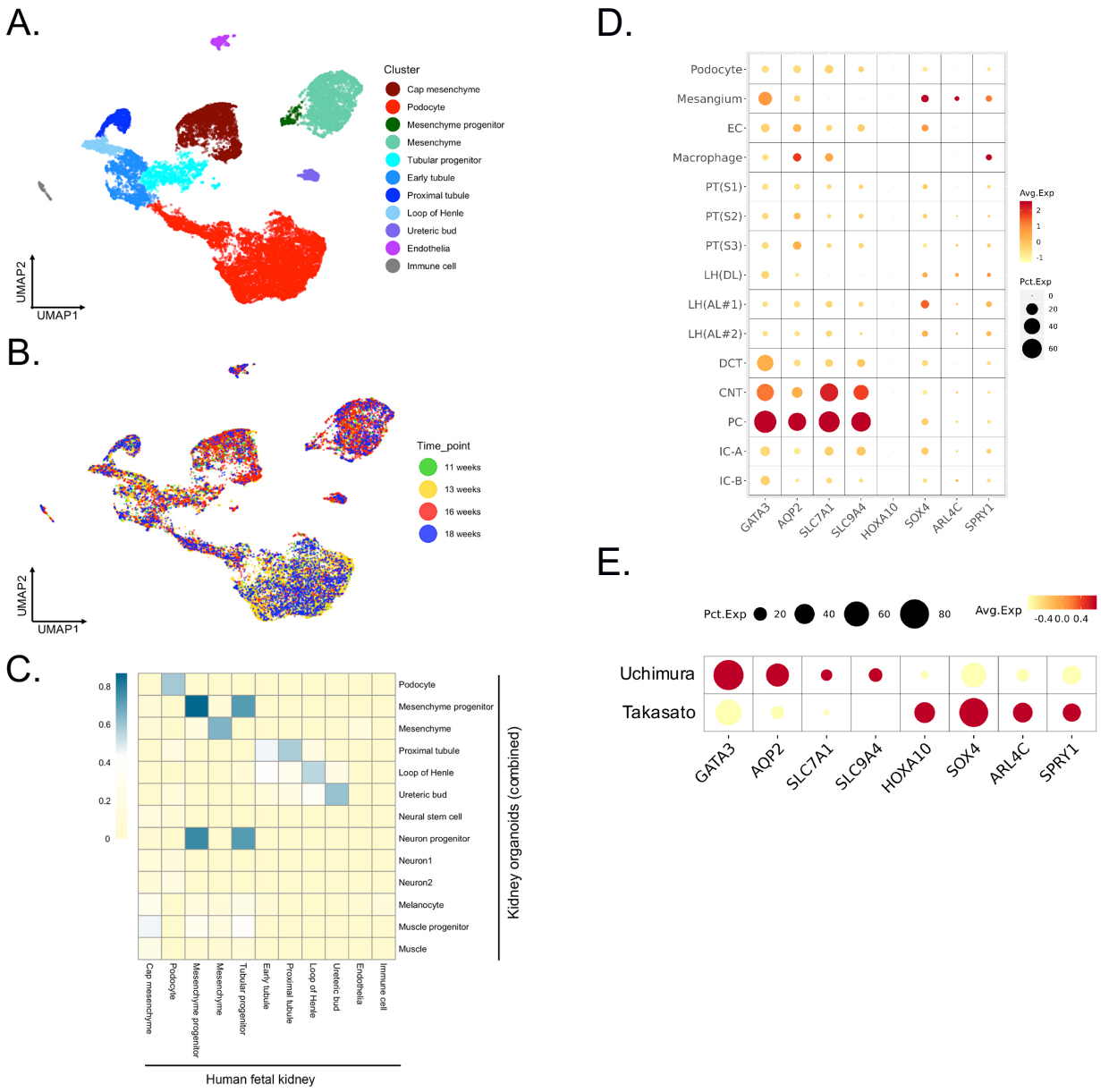

Supplemental Figure S5. Comparison of organoid-derived cell types with fetal kidney cell types and comparison of principal cell markers to organoid-derived principal cells. Related to Figure 4. A. Co-projection by UMAP of human fetal kidney from 11, 13, 16 and 18 weeks. Data is from GSE114530. **B.** Contribution of each timepoint to each cluster. **C.** Pearson's correlation of kidney organoid cell types to human fetal kidney cell types. **D.** Expression levels for markers of mature and developmental principal cells were queried across cell types from an adult human kidney. scRNA-seq data is from GSE118184. **E.** Dotplot showing enhanced expression of principal cell differentiation markers (*GATA3*, *AQP2*, *SLC7A1*, *SLC9A4*) in Uchimura vs. Takasato principal cells. Takasato principal cells express higher levels of developmental genes (*HOXA10*, *SOX4*, *ARL4C*, *SPRY1*).

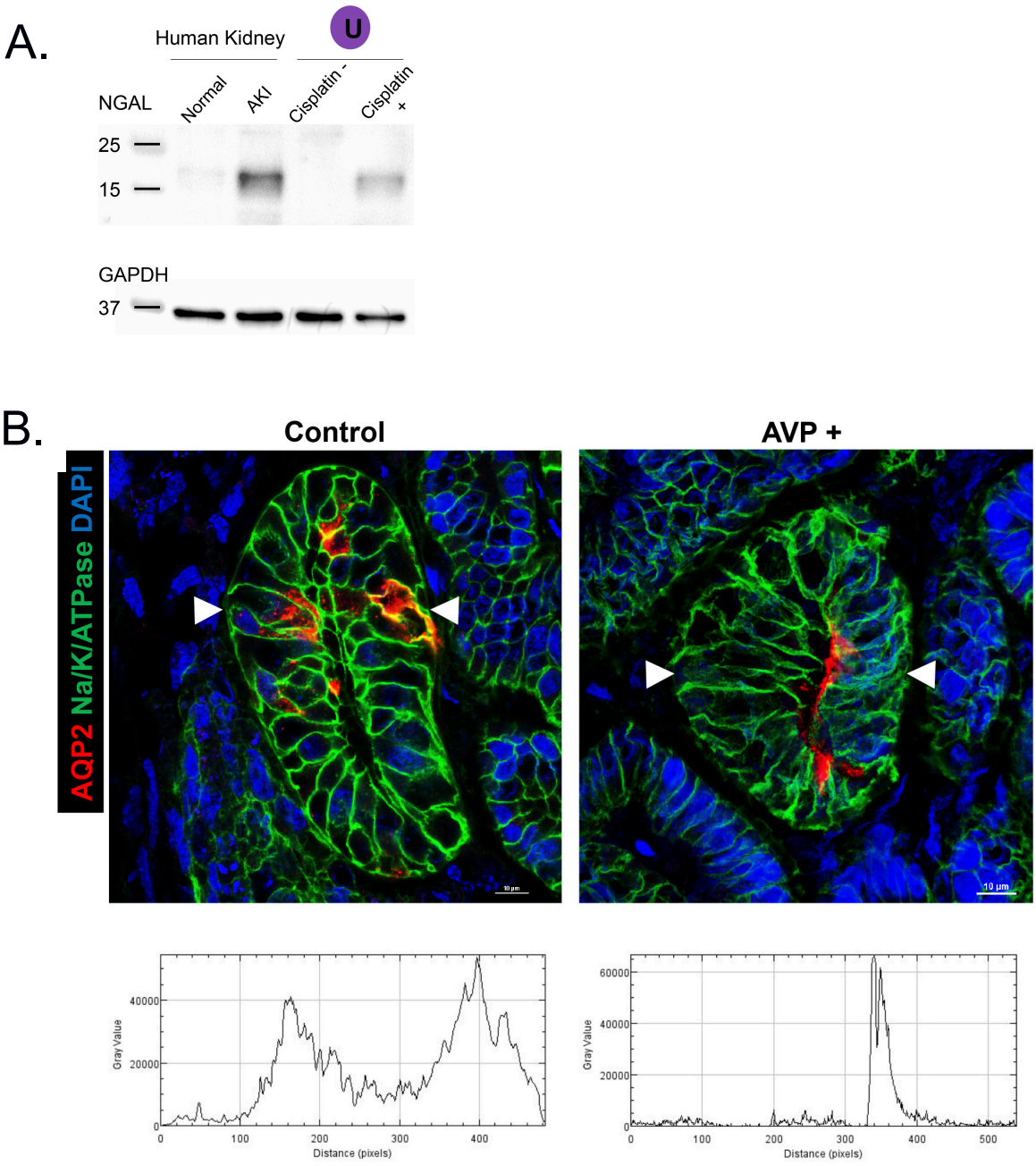

Supplemental Figure S6. Cisplatin induces NGAL protein in kidney organoids and example of AQP2 membrane insertion quantification. Related to Figure 6. A. Western blot of a healthy human kidney and an acute kidney injury human kidney lysate probed for NGAL is included as a positive control. NGAL protein is undetectable in control organoids but upregulated by Cisplatin exposure. **B.** AQP2 fluorescence intensity was quantified in between basolateral membrane anchors (arrowheads). The distance from the apical membrane to the AQP2 peak intensity was divided by the distance from the apical membrane to the basolateral membrane. Scale bar 10 μm.